Available online at www.sciencedirect.com
SCIENCE DIRECT®
ELSEVIER
European Journal of Mechanics B/Fluids 22 (2003) 3–26
EUROPEAN JOURNAL OF MECHANICS B/FLUIDS

Nonlinear oscillations in three-armed tubes

Katsuya Hirata [a], Alex D.D. Craik [b,*]

[a] *Department of Mechanical Engineering, Doshisha University, Kyoto 610-0321, Japan*
[b] *School of Mathematics and Statistics, University of St Andrews, St Andrews, Fife KY16 9SS, Scotland, UK*

Received 25 March 2002; accepted 11 October 2002

Abstract

We consider nonlinear gravitational oscillations of inviscid liquid in arrangements of three tubes joined at their bases, for which the dynamical system is four-dimensional and conservative. Though the problem of two joined tubes was solved in 1738, that of three tubes appears to have remained unstudied. We consider both weakly-nonlinear theory, which gives rise to coupled amplitude evolution equations; and also full numerical solutions. In this way, an understanding is reached of the strengths and limitations of the weakly-nonlinear approximation. Both the weakly-nonlinear approximation and the full system display amplitude modulations on a slow timescale; but only the full system captures a narrow region of chaos.

1. Introduction

The gravitational oscillation of a liquid in two connected tubes, or a U-shaped tube, was one of the first topics of fluid mechanics to receive successful theoretical treatment, the essential theory being set out by Daniel Bernoulli in his *Hydrodynamica* [1] of 1738. It is therefore surprising that a satisfactory theory of oscillations in arrangements of *three* coupled tubes has apparently not yet been developed. This gap in our knowledge is all the more remarkable, given the huge attention paid to nonlinear oscillations in recent decades.

This paper considers the basic inviscid theory of such oscillations, which comprise a four-dimensional conservative dynamical system; and it describes the solutions of this system, both analytically and numerically. Explicit solutions are given for *weakly*-nonlinear oscillations: these are closely related to other well-known dynamical systems, including coupled pendula and standing water waves in a closed container. Corresponding numerical solutions are also described: these extend to strongly-nonlinear oscillations beyond the reach of asymptotic theories. The latter shed considerable light on the accuracy and range of validity of the weakly-nonlinear approximation.

We comprehensively examine three identical straight tubes of uniform cross-section, inclined at equal angles to the vertical, and suitably joined at their bases without any preferential bias. Later, we briefly generalise the formulation to tubes of differing lengths, cross-sections and angles of inclination; and we draw attention to the possible existence of second-harmonic resonance in suitable configurations.

Although our study is here restricted to an unforced and undamped system, which therefore cannot be realised exactly in an experiment, it has several claims to novelty. Our simple three-tube geometry provides an alternative to much-studied coupled-pendulum and water-wave models of low-dimensional dynamical systems. It has the major advantage over water waves in closed containers that additional spatial modes with neighbouring frequencies do not exist. Consequently, the analysis can be pursued to large amplitudes without fear of additional modal complications. Also, fully-nonlinear numerical solutions are far easier to obtain in our system, than they are for free-boundary water-wave problems. Our comparison of full computations and

* Corresponding author.
E-mail address: addc@st-andrews.ac.uk (A.D.D. Craik).

0997-7546/02/$ – see front matter
doi:10.1016/S0997-7546(02)00003-1

weakly-nonlinear theory allows a greater appreciation of the strengths and limitations of the latter, and provided a good check on the accuracy of the former.

Future work incorporating forcing and damping, and with other resonant or near-resonant configurations, is likely to yield valuable results verifiable with quite simple laboratory apparatus.

2. Three equal tubes: formulation

2.1. Basic equations

We consider three identical vertical tubes, having uniform cross-section, and joined at their bases in a smooth and unbiassed manner, as shown in Fig. 1. In equilibrium, the length of each tube filled with inviscid liquid is equal to L, which is supposed much larger than the cross-sectional radius of the tubes. It is then permissible to assume that the motion is uniform across the cross-section. During motion, the upwards displacements of the liquid-air interface in each tube are denoted by $X_j(t')$ ($j = 1, 2, 3$), where t' denotes real time. It is convenient to non-dimensionalise these displacements, and time t', as

$$x_j(t) \equiv \frac{X_j(t')}{L}, \quad t \equiv t'\sqrt{\frac{g}{L}},$$

where g is gravitational acceleration.

The governing equations for the motion may be derived by using Bernoulli's theorem for time-dependent flow or, equivalently, by constructing the Lagrangian and then applying Lagrange's equations. For brevity, we here adopt the latter method. If the level of zero potential energy is taken to be that of rest, with all $x_j = 0$, then the dimensionless potential energy $V(x_j)$ is given by

$$2V(x_j) = {x_1}^2 + {x_2}^2 + {x_3}^2 = \sum_{j=1}^{3} {x_j}^2.$$

Also, the dimensionless kinetic energy $T(\dot{x}_j, x_j)$ satisfies

$$2T(\dot{x}_j, x_j) = \sum_{j=1}^{3} {\dot{x}_j}^2(1 + x_j),$$

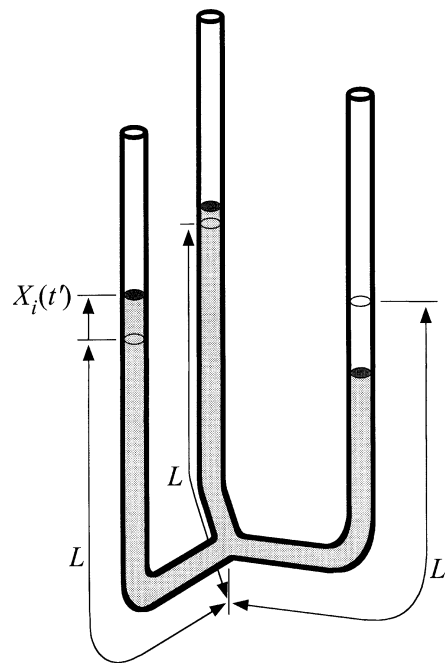

Fig. 1. Three equal vertical tubes.

since the dimensionless length of fluid in each tube at each instant is $1+x_j$. Also, by continuity, $x_1+x_2+x_3=0$, and similarly for their time-derivatives.

Accordingly, the Lagrangian $L \equiv T - V$ may be expressed as a function of any two of x_j and their time-derivatives. On choosing to eliminate x_3, and constructing Lagrange's equations

$$\frac{\mathrm{d}}{\mathrm{d}t}\left[\frac{\partial L}{\partial \dot{x}_j}\right] = \frac{\partial L}{\partial x_j} \quad (j=1,2),$$

we obtain

$$\ddot{x}_1(2-x_2) + \ddot{x}_2(1-x_1-x_2) = \dot{x}_1\dot{x}_2 + \frac{1}{2}\dot{x}_2{}^2 - 2x_1 - x_2, \tag{1}$$

$$\ddot{x}_2(2-x_1) + \ddot{x}_1(1-x_2-x_1) = \dot{x}_2\dot{x}_1 + \frac{1}{2}\dot{x}_1{}^2 - 2x_2 - x_1. \tag{2}$$

An alternative form of these is

$$\ddot{x}_1 + x_1 + \frac{1}{3}(x_1\ddot{x}_1 - x_1\ddot{x}_2 - x_2\ddot{x}_1 - 2x_2\ddot{x}_2) + \frac{1}{6}\left(\dot{x}_1{}^2 - 2\dot{x}_1\dot{x}_2 - 2\dot{x}_2{}^2\right) = 0, \tag{3}$$

$$\ddot{x}_2 + x_2 + \frac{1}{3}(x_2\ddot{x}_2 - x_2\ddot{x}_1 - x_1\ddot{x}_2 - 2x_1\ddot{x}_1) + \frac{1}{6}\left(\dot{x}_2{}^2 - 2\dot{x}_2\dot{x}_1 - 2\dot{x}_1{}^2\right) = 0. \tag{4}$$

An invariant of these equations is the total energy $T+V \equiv E$ say, given by

$$2E = \dot{x}_1{}^2(2-x_2) + \dot{x}_2{}^2(2-x_1) + 2\dot{x}_1\dot{x}_2(1-x_1-x_2) + 2x_1{}^2 + 2x_2{}^2 + 2x_1x_2. \tag{5}$$

Eqs. (3), (4) immediately show that, in the linear approximation with sufficiently small x_1 and x_2, there are two independent modes with

$$\ddot{x}_j + x_j = 0 \quad (j=1,2),$$

which have sinusoidal solutions with dimensionless period $\tau = 2\pi$. At the linear level, such oscillations may comprise *any* mix of x_1, x_2 and x_3 which satisfies continuity. (However, if the three tubes were not identically situated, the frequencies of the two linear modes need not be identical, and the present degeneracy is destroyed, as explained in Section 5.)

2.2. 2-dimensional reduction

The nonlinear equations (1), (2) yield an obvious reduction to a two-dimensional special case with $x_1 = x_2$; and it is easily verified that similar reductions exist for $x_1 = x_3$ (i.e., $2x_1 + x_2 = 0$) and for $x_2 = x_3$ (i.e., $x_1 + 2x_2 = 0$), as they must, by symmetry. The governing equation with $x_1 = x_2 \equiv x$ is then

$$\ddot{x}(1-x) - \frac{1}{2}\dot{x}^2 + x = 0, \tag{6}$$

for which exact solutions are available.

On writing $y \equiv \dot{x}$, we obtain curves in the phase plane (x, y) with

$$\frac{\mathrm{d}}{\mathrm{d}x}\left[(x-1)y^2\right] = 2x,$$

which has the solutions

$$y = \pm\sqrt{\frac{a^2 - x^2}{1-x}} \quad \text{(arbitrary } a\text{)}. \tag{7}$$

Corresponding computer plots are shown in Fig. 2. The case $a^2 = 1$ gives the parabola $y^2 = 1 + x$. It is clear that meaningful solutions exist only when $|x| \leqslant a \leqslant 1$, since no tube can be allowed to empty completely. But this is not enough: since $x_3 = -(x_1 + x_2) = -2x$, we actually need $|x| \leqslant a \leqslant 1/2$. This means that the limiting case with largest oscillations is that shown in Fig. 2 passing through $x = 0.5$ when $y = 0$.

The time-dependence of x is found from

$$\mathrm{d}t = \pm\sqrt{\frac{1-x}{a^2-x^2}}\,\mathrm{d}x,$$

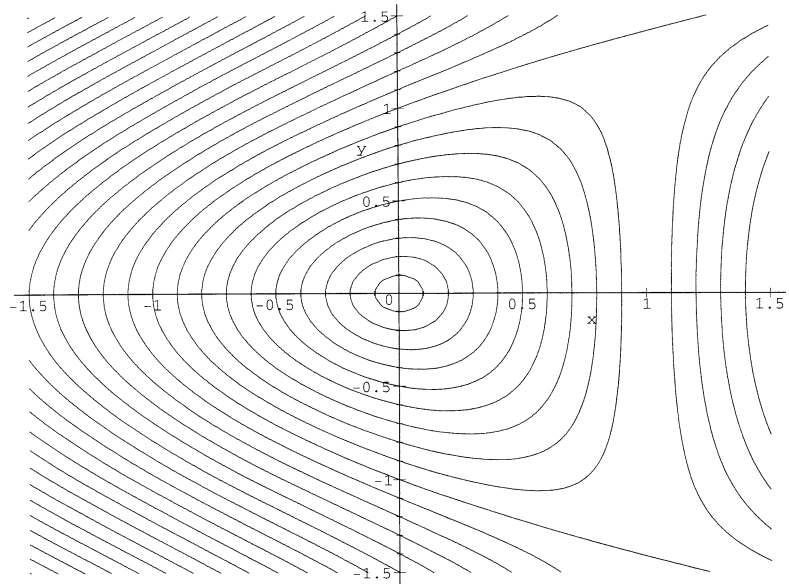

Fig. 2. Solutions in 2-dimensional-reduction case.

and so the period τ is

$$\tau = 2\int_{-a}^{a} \sqrt{\frac{1-x}{a^2-x^2}}\,\mathrm{d}x = 4\sqrt{1+a}\,E(k), \quad k \equiv \sqrt{\frac{2a}{1+a}}. \tag{8}$$

Here, $E(k)$ is the complete elliptic integral of the second kind,

$$E(k) = \int_0^{\pi/2} \sqrt{1-k^2\sin^2 u}\,\mathrm{d}u,$$

see for example Gradshteyn and Ryzhik [2] (result 3.141.2 on p. 231 and p. 905), and Abramowitz and Stegun [3, p. 590]. To recover this result, one needs the substitution $\sin^2 u = (x+1)/2a$. The tables of Abramowitz and Stegun (p. 618) [3] show that $E(k)$ slowly decreases in magnitude, from $\pi/2$ to 1, as k^2 (their $\sin^2\alpha$) increases from 0 to 1. When $a = 1/2$, $k^2 = 2/3$ and $E(k)$ is about 1.261. Therefore, the dimensionless period of small oscillations ($a = k = 0$) is exactly 2π; and that of the largest possible oscillations ($a = 1/2$, $k^2 = 2/3$) is $\tau_{\max} \approx 6.179$, which is only about 1.7% less than 2π.

The above result is exactly the same as that obtained for oscillations in a U-tube with one arm having twice the cross-section of the other. In contrast, oscillations in a U-tube having identical arms are purely sinusoidal with dimensionless period 2π, whatever the amplitude of oscillation.

3. Weakly-nonlinear theory

When nonlinear terms are sufficiently small, with each x_i proportional to a small parameter ε, we may develop a perturbation expansion of form

$$x_1 = \varepsilon A_1 \exp(\mathrm{i}t) + \varepsilon^2\big(B_1\exp(2\mathrm{i}t) + C_1\big) + \text{c.c.} + \text{h.o.t.}, \tag{9}$$

$$x_2 = \varepsilon A_2 \exp(\mathrm{i}t) + \varepsilon^2\big(B_2\exp(2\mathrm{i}t) + C_2\big) + \text{c.c.} + \text{h.o.t.}, \tag{10}$$

where "c.c." denotes complex conjugate and "h.o.t." denotes higher-order terms which are $\mathrm{O}(\varepsilon^3)$ or smaller. Each of the A_j, B_j, C_j $(j = 1, 2)$ are complex-valued functions of the slow dimensionless timescale $T \equiv \varepsilon^2 t$. The procedure is fairly lengthy but straightforward, and details need not be given: see, for example, the textbook of Nayfeh [4, Chapter 6], or the papers of Nagata [5] and Umeki [6] for analogous problems in fluid mechanics. The functions B_j and C_j are found in terms of the A_j from the $\mathrm{O}(\varepsilon^2)$ equations; and these appear in the $\mathrm{O}(\varepsilon^3)$ equations.

Secular growth in $t\exp(\pm \mathrm{i}t)$ is suppressed in the latter by suitably choosing the T-derivatives of the A_j. These turn out to be given by

$$2\mathrm{i}\frac{\mathrm{d}A_1}{\mathrm{d}T} = A_1\big(a|A_1|^2 + b|A_2|^2\big) + cA_2|A_1|^2 + d{A_2}^2\bar{A}_1 + e{A_1}^2\bar{A}_2, \tag{11}$$

$$2\mathrm{i}\frac{\mathrm{d}A_2}{\mathrm{d}T} = A_2\big(a|A_2|^2 + b|A_1|^2\big) + cA_1|A_2|^2 + d{A_1}^2\bar{A}_2 + e{A_2}^2\bar{A}_1, \tag{12}$$

where a, b, c, d and e are real numbers, and the overbar denotes complex conjugate. Although the *form* of these equations was to be expected from general considerations, the values of the coefficents can only be determined by performing the detailed analysis here suppressed. These values were found to be

$$a = -\frac{1}{6}, \quad b = -1, \quad c = \frac{1}{3}, \quad d = \frac{5}{6}, \quad e = -\frac{1}{2}. \tag{13}$$

A useful check on our working is supplied by applying the symmetry transformation $[A_1, A_2, -A_1 - A_2] \to [A_2, -A_1 - A_2, A_1]$ to Eqs. (11), (12). In order to recover identical equations for $\mathrm{d}A_1/\mathrm{d}T$ and $\mathrm{d}A_2/\mathrm{d}T$, it is found to be necessary that $a = 2e + d$, $b = 2e$ and $c = e + d$: conditions which are satisfied by (13). Such a check also rules out the possibility of additional terms $f|A_2|^2A_2$ in (11) and $f|A_1|^2A_1$ in (12), since it turns out that the coefficient f must be zero.

It is relevant to note here the close similarity of the present work to that on water waves in an annular container. This has been studied, with the addition of Faraday oscillatory forcing and weak damping, by Douady, Fauve and Thual [7] who performed both an instructive experiment and weakly-nonlinear theory based on symmetry arguments. Douady, Fauve and Thual found pure-periodic standing waves; periodic clockwise and anti-clockwise propagating travelling waves; and slowly-modulating states resembling these periodic ones. Here, we discover close analogues of this behaviour: our FP1 solutions are analogous to the standing waves of [7], and our FP2 solutions with $\Theta = 2\pi/3, 4\pi/3$ are analogous to their clockwise and counter-clockwise propagating waves (for notation, see below).

For related general theoretical developments employing group transformations and bifurcation theory, see for example Danglemayr and Knobloch [8] or Golubitsky, Stewart and Schaeffer [9]. However, the general formulation of the latter, for systems with D_3 symmetry, differs substantially from that employed here and direct comparison is not easy. We have no bifurcation parameter and our system is Hamiltonian. Furthermore, it was convenient to eliminate one of our variables, x_3, by means of the continuity equation; and the 'variable-mass' nature of our equations make them less simple to express in the standard form of [9]. Nevertheless, several features of our results conform with the generic behaviour predicted in [9]: in particular, in-phase periodic solutions and others with $2\pi/3$ phase-shifts: cf. [9] (pp. 390–394). Further investigation of these similarities would be desirable, but this is not pursued here.

From Eq. (5), the energy is

$$E = \varepsilon^2\big[4\big(|A_1|^2 + |A_2|^2\big) + 2(A_1\bar{A}_2 + A_2\bar{A}_1)\big] + \mathrm{O}\big(\varepsilon^3\big),$$

which is just $\widetilde{E} \equiv ({x_1}^2 + {x_2}^2 + {x_3}^2)/2 + (\dot{x}_1^2 + \dot{x}_2^2 + \dot{x}_3^2)/2$ correctly to $\mathrm{O}(\varepsilon^2)$, as it must be. On writing the A_j in polar form as

$$A_1 \equiv r_1\exp(\mathrm{i}\theta_1), \qquad A_2 \equiv r_2\exp(\mathrm{i}\theta_2),$$

we have

$${r_1}^2 + {r_2}^2 + r_1r_2\cos(\theta_1 - \theta_2) = \frac{\widetilde{E}}{4\varepsilon^2} \equiv F \tag{14}$$

at leading order.

Eqs. (11) and (12) may be recast in terms of r_1, r_2 and $\Theta \equiv \theta_1 - \theta_2$ as

$$2\frac{\mathrm{d}r_1}{\mathrm{d}T} = (e - c){r_1}^2r_2\sin\Theta - dr_1{r_2}^2\sin 2\Theta, \tag{15}$$

$$2\frac{\mathrm{d}r_2}{\mathrm{d}T} = (c - e){r_2}^2r_1\sin\Theta + dr_2{r_1}^2\sin 2\Theta, \tag{16}$$

$$2\frac{\mathrm{d}\Theta}{\mathrm{d}T} = \big({r_1}^2 - {r_2}^2\big)\big[(b - a) + d\cos 2\Theta\big]. \tag{17}$$

Note that $d = c - e = a - b = 5/6$.

Fixed points exist for *all* $r_1, r_2 \geqslant 0$ and $\Theta = 0, \pi$ (hereinafter, referred to as FP1). Also, there are fixed points with $\Theta = 2\pi/3, 4\pi/3$ (modulo 2π) and $r_1 = r_2 \equiv r$ (hereinafter, referred to as FP2). In terms of F, the latter have $r = \sqrt{2F/3}$. These fixed-point solutions exhibit no modulations of r_1, r_2 or Θ; but the corresponding solutions for $\tilde{x}_1$, $\tilde{x}_2$, $\tilde{x}_3$ display

nonlinear frequency shifts. For FP1, $\mathrm{d}\theta_1/\mathrm{d}T = \mathrm{d}\theta_2/\mathrm{d}T = F/12$, giving oscillations of the $\tilde{x}_j$ with frequency $1 + \widetilde{E}/48$ on the timescale t; while, for FP2, $\mathrm{d}\theta_1/\mathrm{d}T = \mathrm{d}\theta_2/\mathrm{d}T = F/2$ and the corresponding frequency is $1 + \widetilde{E}/8$. These results will be shown in Section 4.4, where they are compared with full nonlinear results.

It follows from (15), (16) that

$$\frac{\mathrm{d}}{\mathrm{d}T}(2r_1r_2) = dr_1r_2\big({r_1}^2 - {r_2}^2\big)\sin 2\Theta, \qquad \frac{\mathrm{d}}{\mathrm{d}T}\big({r_1}^2 + {r_2}^2\big) = (e-c)r_1r_2\big({r_1}^2 - {r_2}^2\big)\sin\Theta.$$

Also, from the energy equation (14) (which is of course also derivable from (15)–(17)), we have

$$\cos\Theta = \frac{F - {r_1}^2 - {r_2}^2}{r_1r_2} \tag{18}$$

with the energy invariant F determined by the initial conditions. We therefore have

$$(e-c)\frac{\mathrm{d}}{\mathrm{d}T}\big({r_1}^2{r_2}^2\big) = 2d\big(F - {r_1}^2 - {r_2}^2\big)\,\frac{\mathrm{d}}{\mathrm{d}T}\big({r_1}^2 + {r_2}^2\big),$$

from which we obtain the further invariant

$$d\big({r_1}^2 + {r_2}^2 - F\big)^2 + (e-c){r_1}^2{r_2}^2 \equiv G. \tag{19}$$

Here, G must be negative or zero, to ensure that $|\cos\Theta| \leqslant 1$ in (18).

The physical significance of G is also connected with the invariant

$$r_1r_2\sin\Theta = \pm\sqrt{-\frac{6G}{5}},$$

a result easily verified from (18) and (19) on recalling that $d = c - e = 5/6$. This result has a simple geometrical interpretation: the area enclosed by the triangle comprising the origin and the complex numbers A_1, A_2 remains invariant during the modulations of amplitude and phase. In fact, this invariant quantity and the energy invariant F both follow immediately from the constancy of $A_1\bar{A}_2 + A_2\bar{A}_3 + A_3\bar{A}_1$, where $A_3 = -A_1 - A_2$ (as may be verified directly from (11) and (12)). This result may also be deduced by symmetry considerations.

Result (19) ensures that all solution trajectories lie on concentric ellipses in the $({r_1}^2, {r_2}^2)$ plane. These ellipses may be parametrised as

$${r_1}^2 + {r_2}^2 - \frac{4}{3}F = \frac{2}{\sqrt{3}}H\sin\psi, \qquad {r_1}^2 - {r_2}^2 = 2H\cos\psi, \tag{20}$$

where

$$H^2 \equiv \frac{1}{3}F^2 + \frac{6}{5}G > 0$$

and $\psi = \psi(T)$ is yet to be found. The largest ellipse for each fixed F is that with $G = 0$. The common centre of the ellipses is situated at $({r_1}^2, {r_2}^2) = (2F/3, 2F/3)$, the major axis lies along the line ${r_1}^2 + {r_2}^2 = 4F/3$, and the ratio of major to minor axes is $\sqrt{3}$. Both r_1 and r_2 always remain greater than zero, as they must. The ellipses shrink towards a fixed point at the centre as $H \to 0$.

Eq. (17) for Θ becomes

$$\frac{\mathrm{d}(\cot\Theta)}{\mathrm{d}T} = \frac{5}{3}H\cos\psi. \tag{21}$$

On calculating the T-derivative of ${r_1}^2 + {r_2}^2$ from (15) and (16) and using (20), we obtain

$$\frac{2}{\sqrt{3}}H\cos\psi\,\frac{\mathrm{d}\psi}{\mathrm{d}T} = -\frac{5}{6}\big({r_1}^2 - {r_2}^2\big)r_1r_2\sin\Theta = -\frac{5}{3}H\cos\psi\left[\pm\sqrt{-\frac{6}{5}G}\right].$$

Accordingly, $\psi(T)$ is

$$\psi(T) = \mp\sqrt{-\frac{5}{2}G}\,T + \psi_0 \quad (\psi_0 \text{ constant}) \tag{22}$$

and it follows that

$$\cot\Theta = \pm\frac{\sqrt{10}}{3}\,\frac{H}{\sqrt{-G}}\left(\sin\psi + \frac{1}{2\sqrt{3}}\,\frac{F}{H}\right). \tag{23}$$

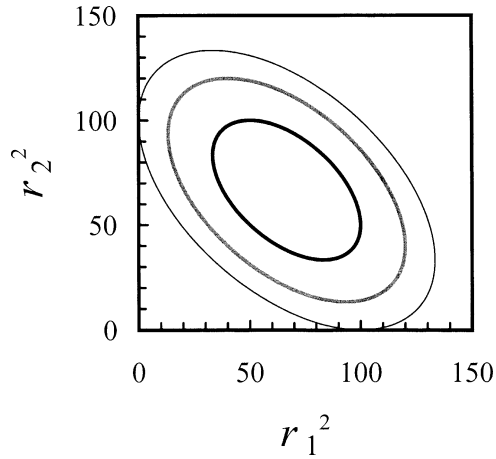

Fig. 3. Trajectories on the plane $\{{r_1}^2, {r_2}^2\}$ for $F = 100$. Black thin line (the largest ellipse), $G = -0.9$; grey thick line (medium ellipse), -1000; black thick line (the smallest ellipse), -2000.

The slow amplitude modulations are fully given by the above results. In the original dimensionless time t, the period of such modulations is clearly $2\pi\sqrt{-2/5G}\,\varepsilon^{-2}$.

Some examples are shown in Fig. 3, which are computed directly from Eqs. (15)–(17), and which coincide with ellipses of Eq. (20). Each ellipse is determined by F and G only. The ellipses shown, and the time-periods required to traverse them, agree with the analytical results just given. The centre of the ellipses is at $({r_1}^2, {r_2}^2) = (200/3, 200/3)$, which is the fixed point FP2 for $F = 100$.

4. Direct computations

The full equations (3), (4) are amenable to direct computations on a personal computer. Our adopted numerical method is a classic Runge–Kutta method, or a four-stage explicit method, with numerical accuracy of double precision. In most cases, the time steps, which were controlled so as to keep the total energy E constant with relative error less than 10^{-12}, were about 10^{-3}. In test cases, we confirmed that the results with the time step of about 10^{-3} are the same as with one of about 10^{-4}.

Our fully-nonlinear computations provide interesting comparisons with the weakly-nonlinear theory described above. Such direct comparison is far less easy in other physical contexts of mode-interaction: for instance, fully-nonlinear computations of interacting standing waves on liquid interfaces are notoriously hard to do. But, here, the nonlinear terms are much more amenable; and the physical restriction to oscillations in three tubes rules out the appearance of other spatial modes, which is a common phenomenon at fluid interfaces: see, for example Craik [10] and Decent and Craik [11].

With three identical tubes, there is a single basic frequency of oscillations which is surprisingly insensitive to their amplitude: in a 2-dimensional-reduction case, we found above that the largest possible oscillations have frequencies only about 1.7% less than those of small-amplitude linear disturbances, and even in other cases, it is only several per cent less (see Section 4.4). On the other hand, large-amplitude oscillations are not sinusoidal; but weakly-nonlinear theory supposes that they are sinusoidal at leading order in the small amplitude parameter ε. It is therefore unlikely that weakly-nonlinear theory yields satisfactory approximations at large amplitudes: certainly, it cannot do so either for waves on liquid interfaces or for coupled pendula, where similar weakly-nonlinear equations arise.

To enable comparison with weakly-nonlinear theory, we write

$$x_j = \varepsilon r_j^* \exp\bigl[\mathrm{i}(t + \theta_j^*)\bigr] + \text{c.c.} \quad (j = 1, 2), \tag{24}$$

and solve Eqs. (3), (4) numerically, imposing, without loss of generality, the initial condition $\dot{x}_1 = 0$ and $\theta_1^* = 0$ at $t = 0$. Thus, initially, we have

$$x_{10} = 2\varepsilon r_{10}^*, \qquad \dot{x}_{10} = 0,$$
$$x_{20} = 2\varepsilon r_{20}^* \cos\theta_{20}^*, \qquad \dot{x}_{20} = -2\varepsilon r_{20}^* \sin\theta_{20}^*,$$

where subscript 0 denotes evaluation at $t = 0$.

In the weakly-nonlinear limit, $r_1^*,\ r_2^*,\ \theta_1^*$ and θ_2^* reduce to $r_1,\ r_2,\ \theta_1$ and θ_2 of the previous section. We shall also calculate quantities $F^*,\ G^*,\ H^*$ and Θ^* defined as in the expressions above for $F,\ G,\ H$ and Θ, but with $r_1^*,\ r_2^*,\ \theta_1^*$ and θ_2^* instead of $r_1,\ r_2,\ \theta_1$ and θ_2.

The above initial conditions, and so the subsequent solution, are parametrised by $\varepsilon r_{10}^*,\ \varepsilon r_{20}^*$ and θ_{20}^*; but it is preferable to use an equivalent parametrisation in terms of $E = E_0 = const.$, $\Theta_0^* \equiv \theta_{10}^* - \theta_{20}^*$ and $k_0^* \equiv r_{20}^*/r_{10}^*$. Here, E is the constant energy of (5), *not* the weakly-nonlinear approximation $\widetilde{E}$ in (14). It will also be convenient to restrict $\cos\theta_{20}^*$ to be positive, but allow k_0^* to have either sign. (We could also have set $r_{10}^* = 1$, so defining 2ε to be x_{10}: but there is no advantage in doing so, since ε and r_{10}^* always appear in combination.)

In the following, we first describe several particular types of solution, and then the general class.

4.1. Type 1a and Type 1b: singly-periodic solutions

There are two kinds of exactly periodic solutions. Here, we call them Type 1a and Type 1b. As will be shown, Type 1a and Type 1b are non-modulating special cases of Type 3 and Type 2, respectively.

An example of Type 1a is solutions with parameters $\Theta_0^* = 0$, $k_0^* = 1$, which correspond to the 2-dimensional reduction of Section 2.2. The solutions have phase portraits in complete agreement with Fig. 2. These are also a special case of the weakly-nonlinear fixed points FP1. Here, the quantities $\varepsilon^4 G^*$ and Θ^* remain zero for all t; but $\widetilde{E}^* \equiv 4\varepsilon^2 F^*$ and $\varepsilon^4 H^{*2}$ are not constant, as in weakly-nonlinear theory. Instead, they display temporal fluctuations, which are stronger at greater amplitudes because of the increasing contributions of higher harmonics. Of course, the *actual* energy of (5) is constant; but this is estimated in (14) using weakly-nonlinear theory. Fig. 4 shows one such case, for $E = 1.5$: the amplitudes here are quite large, with noticeably sharpened peaks for $x_1 = x_2$, and so sharpened troughs for $x_3 = -2x_1$. This case turns out to have maxima and minima of x_3 beyond ± 1 and so is physically unrealisable; but realisable cases with maximum amplitudes close to 1 are not much different. Equivalent 2-dimensional periodic solutions occur for $\Theta_0^* = 0$, $k_0^* = -0.5$ and -2: these have oscillations with $x_2 = x_3$ and $x_1 = x_3$ respectively.

An example of Type 1b is shown in Fig. 5 with parameters $(E, \Theta_0^*, k_0^*) = (0.42, 4.34, 1.39)$. These values are quite close to FP2 $(0.42, 4\pi/3, 1)$ of weakly-nonlinear theory; but the exact solution with the latter values shows some modulation. Identical time histories with sharpened troughs appear cyclically in the order of $x_3,\ x_2$ and x_1. Type 1b obviously corresponds to the weakly-nonlinear fixed points FP2, although there is some deviation from weakly-nonlinear theory because of variations in $\varepsilon^4 G^*,\ \Theta^*,\ \widetilde{E}^*\ (\equiv 4\varepsilon^2 F^*)$ and $\varepsilon^4 H^{*2}$. Equivalent FP2 periodic solutions occur for $\Theta_0^* \approx 2\pi/3$, $k_0^* \approx 1$, where identical time histories appear cyclically in the reverse order of $x_1,\ x_2$ and x_3.

4.2. Type 2: out-of-phase modulations

With $\Theta_0^* = -\pi/2$, the initial motion of x_1 and x_2 has a phase difference of $-\pi/2$ or $\pi/2$. Fig. 6 shows an example with $(E, \Theta_0^*, k_0^*) = (0.86, -\pi/2, 3)$. The phase differences between x_1 and x_2 and between x_2 and x_3 fluctuate about a mean close to $-2\pi/3$, and wave forms of $x_1,\ x_2$ and x_3 are very similar. Both these features are similar to Type 1b or the fixed points FP2. But, in addition to the basic period close to 2π, there are slower periodic modulations in amplitude. Corresponding trajectories with smaller values of E show modulations of roughly similar strengths but longer modulation periods. The characteristic feature of Type 2 solutions is that the time-histories of each x_j $(j = 1, 2, 3)$ are closely similar, but shifted relative to each other by one-third of the modulation period.

The period of modulation predicted by weakly-nonlinear theory is $\tau = 2\pi\sqrt{-2/5G^*}/\varepsilon^2$; but now G^* fluctuates because of non-negligible higher-order nonlinear terms. When the amplitudes are small, the fluctuations are unimportant. Even when they

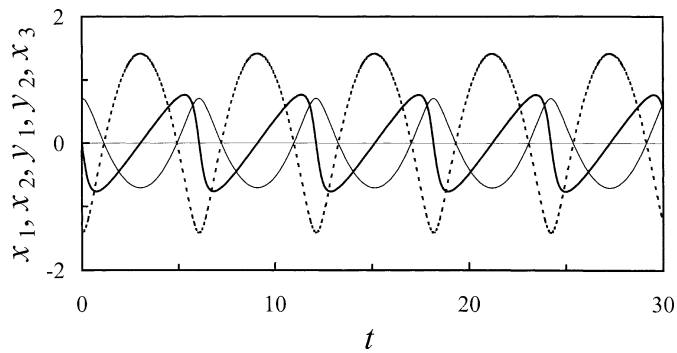

Fig. 4. Time histories of Type 1a for $(E, \Theta_0^*, k_0^*) = (1.5, 0, 1)$. Thin line, x_1 and x_2; thick line, $\dot{x}_1$ and $\dot{x}_2$; dotted line, x_3.

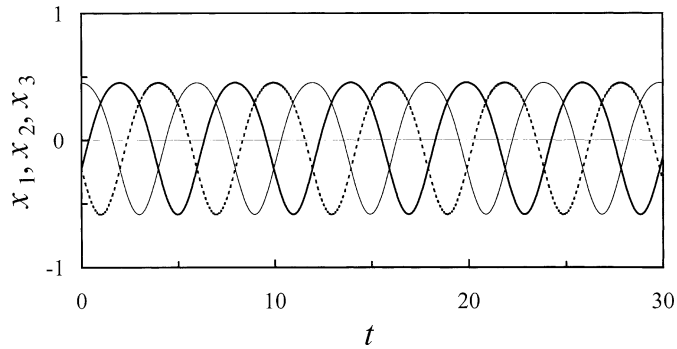

Fig. 5. Time histories of Type 1b for $(E, \Theta_0^*, k_0^*) = (0.42, 4.34, 1.39)$. Thin line, x_1; dotted line, x_2; thick line, x_3.

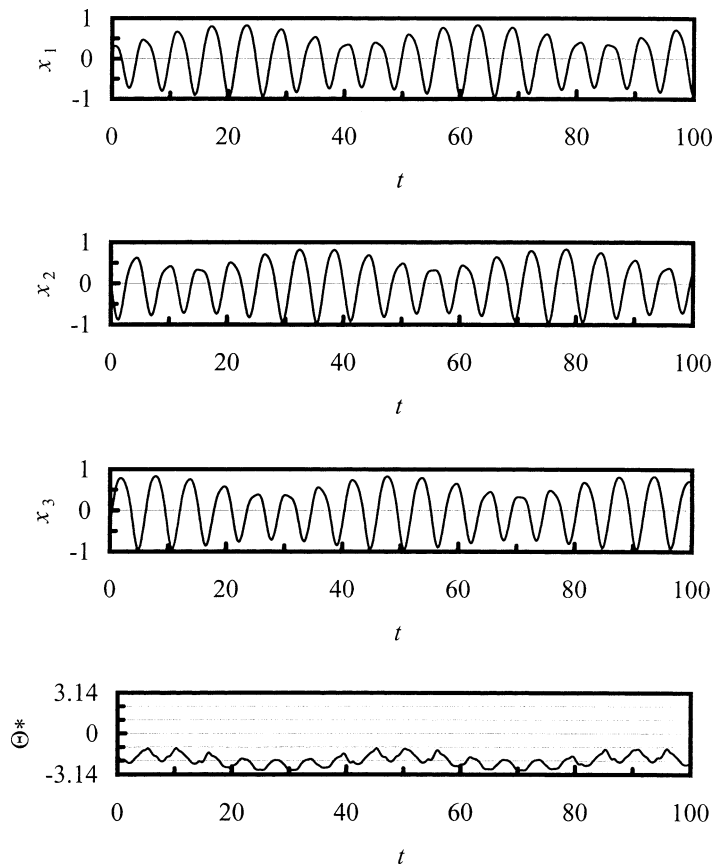

Fig. 6. Time histories of Type 2 for $(E, \Theta_0^*, k_0^*) = (0.86, -\pi/2, 3)$.

are large, we find that the *mean* value of τ agrees quite closely with the modulation period of the computed solutions, as shown in Fig. 7 for the above parameter values. However, in this last case, the estimate of τ based solely on G_0^* ($\equiv$ the value of G^* at $t = 0$), rather than on a time-average, gives a considerable over-estimate of 58, instead of just over 42 which can be obtained from Fig. 6. We conclude that the modulation period predicted by weakly-nonlinear theory is accurate for small amplitudes as expected, and also for large amplitudes, when averaged in this sense; but the latter is not particularly helpful since the full solution must be computed in order to find the average!

Figs. 8(a), 8(b) show corresponding trajectories in the plane $\{(2\varepsilon r_1^*)^2, (2\varepsilon r_2^*)^2\}$: according to weakly-nonlinear theory, these trajectories should be ellipses with centres at $(2\widetilde{E}/3, 2\widetilde{E}/3)$ as described below (20). A weakly-nonlinear fixed point FP2 is at the centre of the ellipse: the equivalent non-modulating solution of Type 1b is also located close to this point, showing not a

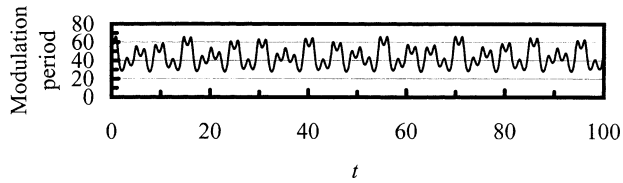

Fig. 7. Amplitude modulation period of Type 2 predicted by weakly-nonlinear theory for $(E, \Theta_0^*, k_0^*) = (0.86, -\pi/2, 3)$.

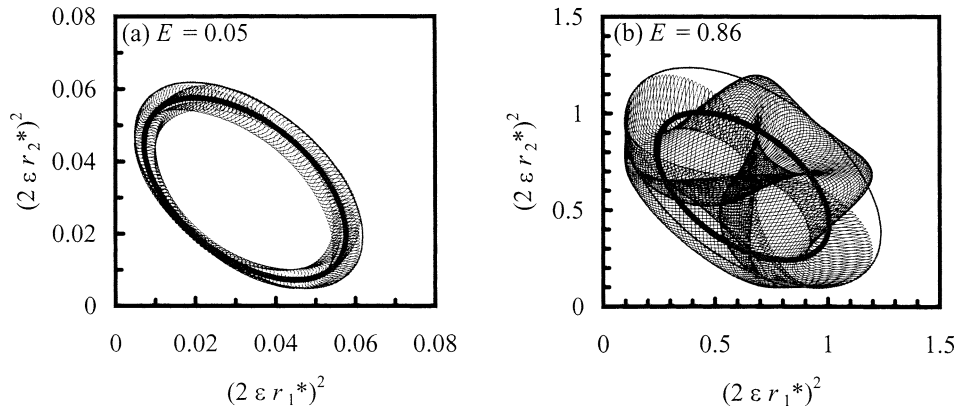

Fig. 8. Trajectory of Type 2 on the plane $\{(2\varepsilon r_1^*)^2, (2\varepsilon r_2^*)^2\}$. (a) $(E, \Theta_0^*, k_0^*) = (0.05, -\pi/2, 3)$, (b) $(E, \Theta_0^*, k_0^*) = (0.86, -\pi/2, 3)$. In each figure, a thin grey line (larger ellipse) denotes the weakly-nonlinear approximation with G_0^*, and a thick grey line (smaller ellipse) denotes that with $\overline{G}^*$.

point but a closed curve because of the presence of higher harmonics. In each figure, two ellipses are shown; the larger ellipse is for the initial value G_0^*, and the smaller is for the time-averaged value $\overline{G}^*$. Here, note that the centres of the two ellipses are not the same, because of fluctuations of F^*, G^* and H^* in contrast with constant F, G and H in the weakly-nonlinear theory. A trajectory in Fig. 8(a) is for quite small amplitudes with $(E, \Theta_0^*, k_0^*) = (0.05, -\pi/2, 3)$ and is close to the two ellipses, but with fairly small superimposed rapid oscillations coming from higher-order terms. In contrast, Fig. 8(b) is for large amplitudes with $(E, \Theta_0^*, k_0^*) = (0.86, -\pi/2, 3)$, being the same case as in Fig. 6. This figure shows large departures from the ellipses of weakly-nonlinear theory, on account of strong higher harmonics, which also cause large fluctuations of both G^* and τ.

4.3. Type 3: in-phase modulations

Fig. 9 shows solutions for $(E, \Theta_0^*, k_0^*) = (1, 0, 3)$. Now, the rapid oscillations of x_1 and x_2 are nearly in phase with period of 2π, as in Type 1a. But, because x_1 and x_2 have differing amplitudes, they modulate in anti-phase on a longer timescale. The modulation of x_3 is very weak, and has half the period of that for x_1 and x_2.

Note that, when x_1 or x_2 becomes small, the second-harmonic component with period π is clearly visible. This component may be understood physically as follows. When the fluid mainly oscillates between (say) tubes 2 and 3, the pressure at the foot of tube 1, as given by Bernoulli's theorem, has a component proportional to the square of the velocity, and this has a dominant frequency twice that of the oscillation.

Fig. 10 gives the corresponding trajectory in the plane $\{(2\varepsilon r_1^*)^2, (2\varepsilon r_2^*)^2\}$: in this case, $G_0^* = 0$ and the fluctuation of G^* is small. It follows that the ellipses predicted by weakly-nonlinear theory with G_0^* and $\overline{G}^*$ are almost the same. Despite a rather large value of E, the trajectory still lies quite close to an arc of these ellipses, having considerable contamination by higher harmonics. In all Type 3 cases, the initial data corresponds to marginally-stable fixed points FP1. The complete ellipse is not traced out, because the modulation period is infinite by weakly-nonlinear theory. Correspondingly, the period of modulations in Fig. 9 is much larger ($\tau \approx 200$) than in Fig. 6 ($\tau = 42$).

4.4. Period of oscillation

The period of oscillation is always quite close to 2π in our fully-nonlinear computations, but differs slightly from this value because of nonlinear effects. We have confirmed that this nonlinear change in the period of oscillation is given very accurately by the weakly-nonlinear approximation.

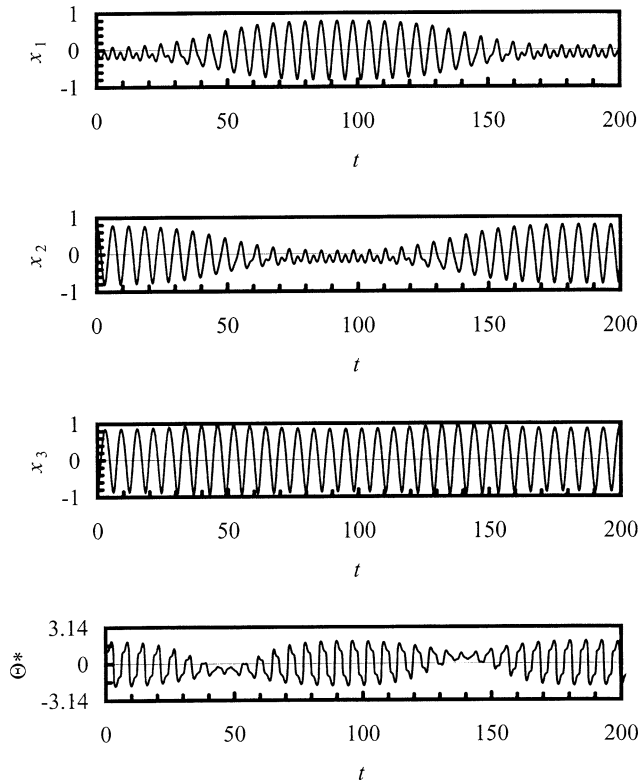

Fig. 9. Time histories of Type 3 for $(E, \Theta_0^*, k_0^*) = (0.7, 0, 9)$.

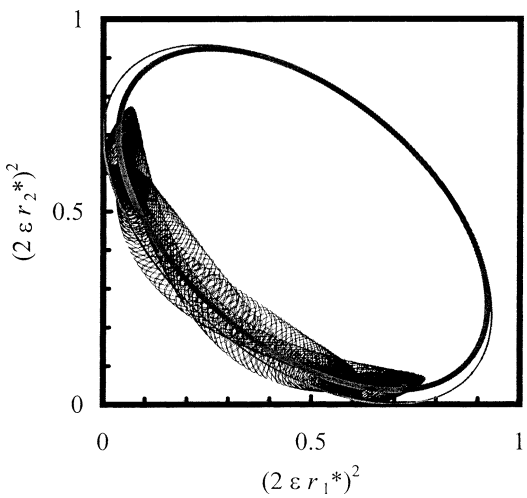

Fig. 10. Trajectory of Type 3 on the plane $\{(2\varepsilon r_1^*)^2, (2\varepsilon r_2^*)^2\}$ for $(E, \Theta_0^*, k_0^*) = (0.7, 0, 9)$. In each figure, a thin grey line (larger ellipse) denotes the weakly-nonlinear approximation with G_0^*, and a thick grey line (smaller ellipse) denotes that with $\overline{G}^*$.

Returning to the formulation of Section 3, we find, after some algebra, that

$$\frac{\mathrm{d}\theta_1}{\mathrm{d}T} = -\frac{G}{r_1^2} + \frac{F}{12}. \tag{25}$$

The average value of this, taken over the modulation period $\tau = 2\pi/\sqrt{-2/5G}$, gives the averaged frequency of A_1, and this estimates the frequency modification of the oscillation of x_1.

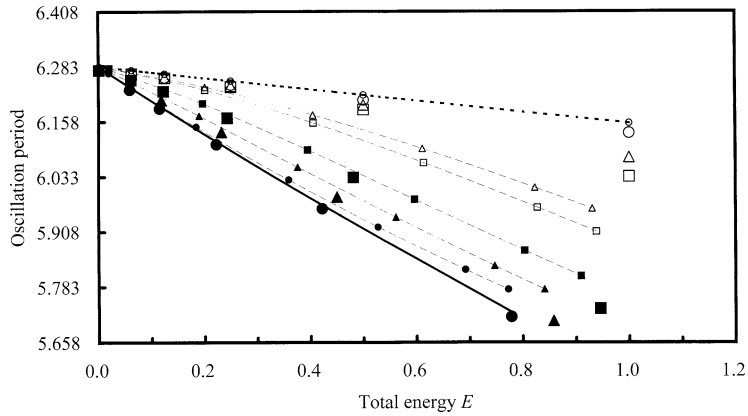

Fig. 11. Oscillation period against E. Larger open circle, $(\Theta_0^*, k_0^*) = (0, 1)$ (in Type 1a); larger solid circle, $(\Theta_0^*, k_0^*) \approx (4\pi/3, 1)$ (in Type 1b); larger solid triangle, $(\Theta_0^*, k_0^*) = (-\pi/2, 3)$ (in Type 2); larger solid square, $(\Theta_0^*, k_0^*) = (-\pi/2, 9)$ (in Type 2); larger open triangle, $(\Theta_0^*, k_0^*) = (0, 3)$ (in Type 3); larger open square, $(\Theta_0^*, k_0^*) = (0, 9)$ (in Type 3). Thick solid line, $16\pi/(\widetilde{E} + 8)$ (the weakly-nonlinear theory for Type 1b or FP2); thick dotted line, $96\pi/(\widetilde{E} + 48)$ (that for Type 1a). Smaller symbols with thin broken lines denote corresponding weakly-nonlinear approximations by Eq. (26) using $\overline{G}^*$ and $\overline{F}^*$.

Now, from Eq. (20),

$$\frac{1}{r_1^2} = \frac{1}{2F/3 + (2H/\sqrt{3})\sin(\psi + \pi/3)}$$

with ψ given by (22). Its average over τ is

$$\frac{\sqrt{3}}{2H} \int_{-\pi/2}^{\pi/2} \frac{\mathrm{d}u}{a + \sin u},$$

where $a = F/\sqrt{3}H$. This is just $1/\sqrt{F^2 - 3H^2}$ (see Gradshteyn and Ryzhik [2, p. 147]). Therefore, the averaged frequency of the oscillations of x_1 is

$$\Omega = 1 + \varepsilon^2 \left\{ \frac{1}{2}\sqrt{-\frac{5G}{2}} + \frac{1}{12}F \right\} \tag{26}$$

according to weakly-nonlinear theory. When $|G| \ll F^2$, a good enough approximation is obtained on omitting the G term. This gives a period $2\pi/\Omega = 96\pi/(\widetilde{E} + 48)$ where $\widetilde{E} \equiv 4\varepsilon^2 F$, which agrees with that for the fixed points FP1 stated in Section 3. Type 3 modulating solutions typically have small values of $|G|$ since $\sin\Theta$ usually remains small. But large enough values of $|G|$ affect the period. In particular, the fixed points FP2 have $\Theta = 2\pi/3$ or $4\pi/3$ (modulo 2π) with quite large $|G|$ and corresponding frequency $1 + \widetilde{E}/8$, as already mentioned in Section 3; and Type 2 modulating solutions have Θ-values which fluctuate about that of FP2. Accordingly, the average oscillatory period of Type 2 solutions tends to be not too far from $16\pi/(\widetilde{E} + 8)$. Some examples, comparing these estimates with the oscillation period obtained from exact computations, are shown in Fig. 11. The agreement is satisfactory, except for Type 3 cases with large amplitudes. Here, in computations, oscillation periods of Type 2 and Type 3 are calculated as mean values over about 1,000 periods, as the period fluctuates with time due to the long-term amplitude modulation.

4.5. The general class: Poincaré sections

Poincaré sections provide another means of describing the solutions. We plot the point (x_1, x_2) each time $\dot{x}_2$ passes through zero. For out-of-phase oscillations of Type 2, where $\Theta_0^* = -\pi/2$, the plot usually falls on two separate closed curves. Fig. 12(a) shows such Poincaré sections with $(E, \Theta_0^*, k_0^*) = (0.5, -\pi/2, k_0^*)$ for various values of k_0^*: except when k_0^* is close to zero, there are two closed curves which are comprised of many black dots (the thin black ellipse and thick grey curves are explained later). In contrast, as in Fig. 12(b), in-phase solutions of Type 3, with $\Theta_0^* = 0$, give plots which are usually two arcs, except when k_0^* is near 0 or -1 (more precisely, $k_0^* \approx 0.0209795$ or -1.02097965). Note the periodic solution for $k_0^* = 1$ (which exists also for $k_0^* = -1/2, -2$), which is of Type 1a. For Type 3, Poincaré sections with k_0^* equal to reciprocal values k^* and $1/k^*$ are indistinguishable, as expected by symmetry.

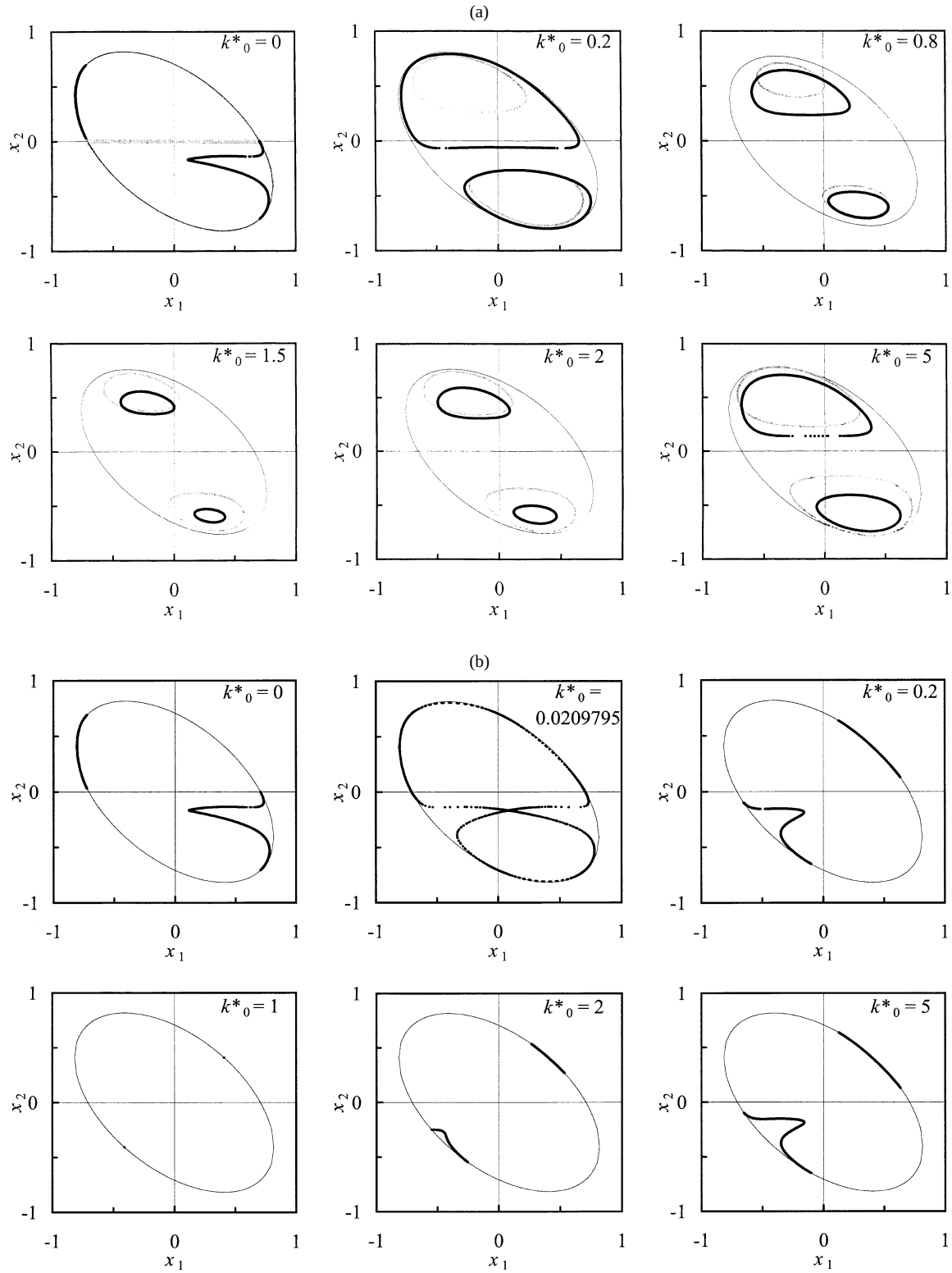

Fig. 12. Poincaré section for $E = 0.5$. (a) $\Theta_0^* = -\pi/2$, (b) $\Theta_0^* = 0$. In each figure, a thin black line (an ellipse) denotes Eq. (27). In figure (a), thick grey lines denote Eq. (31).

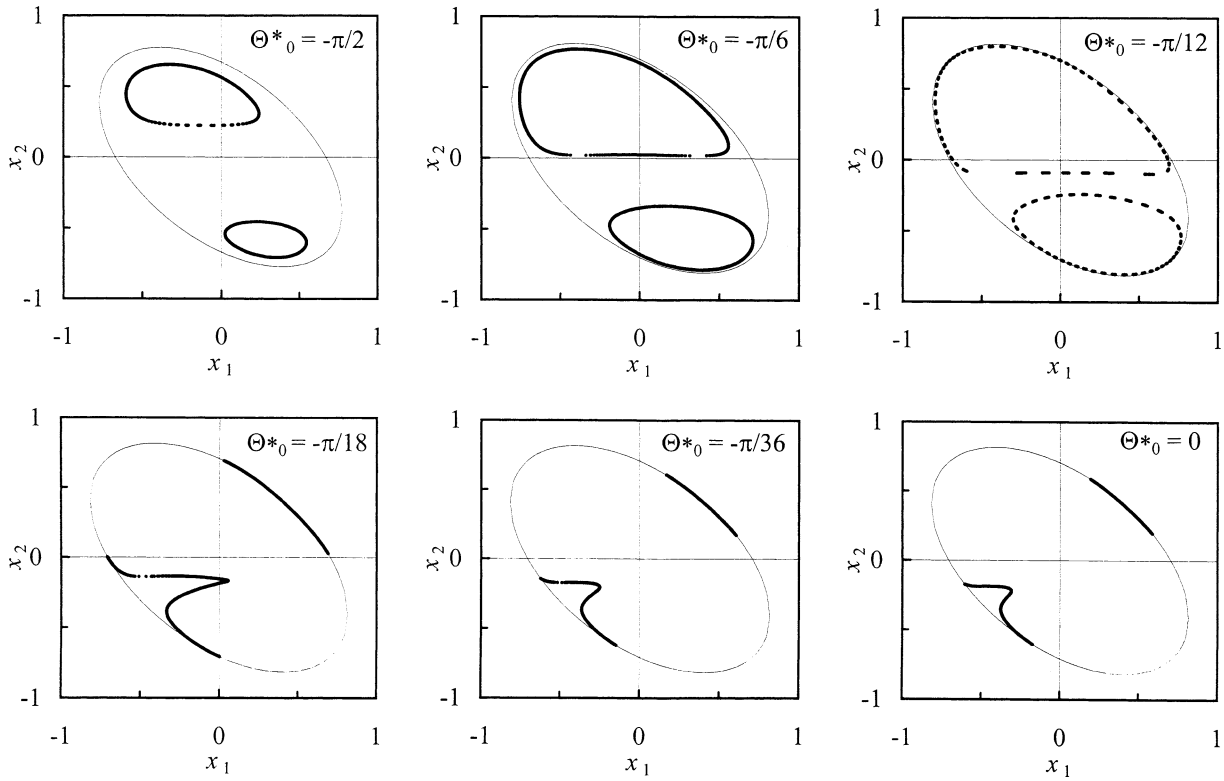

Fig. 13. Poincaré section for $E = 0.5$ and $k_0^* = 3$. In each figure, a thin black line (an ellipse) denotes Eq. (27).

For several other values of Θ_0^* between $-\pi/2$ and 0, Poincaré sections are shown in Fig. 13 for $(E, \Theta_0^*, k_0^*) = (0.5, \Theta_0^*, 3)$. For Θ_0^* far from 0 or $\pm\pi$, these sections are pairs of closed curves; and for values close to 0 or $\pm\pi$, they are pairs of arcs.

On Poincaré sections with $\dot{x}_2 = 0$, it follows from (5) that

$$x_1{}^2 + x_2{}^2 + x_1 x_2 < E,$$

or

$$\frac{3}{4}(x_1 + x_2)^2 + \frac{1}{4}(x_1 - x_2)^2 < E \tag{27}$$

provided $x_2 < 2$ (which it must for all physically-realisable cases). Then, Poincaré sections must all lie inside ellipses with centre at the origin, major axis of diameter $2\sqrt{E}$ along $x_1 = -x_2$, and minor axis of diameter $2\sqrt{E/3}$ along $x_1 = x_2$. These are the large ellipses drawn by thin black lines in Figs. 12, 13, 14 and 18. When Θ_0^* is near 0, $\dot{x}_1$ is usually small whenever $\dot{x}_2$ is zero: then, the sections lie rather close to (and inside) this ellipse or portions thereof. But, for Θ_0^* farther from 0, sections usually lie well inside the ellipse.

To investigate the transition between closed curves and arcs, we consider the case with $(E, \Theta_0^*, k_0^*) = (0.7, 0, k_0^*)$ for small k_0^* (see Fig. 14). Note that, if E is less than or equal to 0.7, x_1, x_2 and x_3 are always less than one. Two pairs of arcs, present for $0 \leqslant k_0^* \leqslant 0.0344$, merge into two joined closed curves for $0.0345 \leqslant k_0^* \leqslant 0.0348$, then again become two pairs of arcs for $k_0^* \geqslant 0.0349$. The range of k_0^* for the merged curves depends on E; for example, $k_0^* \approx 0.0209795$ at $E = 0.5$ (see Fig. 12(b)), $0.01 \leqslant k_0^* \leqslant 0.22$ at $E = 1.4$, and $-0.16 \leqslant k_0^* \leqslant 0.66$ at $E = 2$. Fig. 15 shows the extent of this merged-curve region at $\Theta_0^* = 0$ and $k_0^* \approx 0$, on the (E, k_0^*) plane, within which chaos is observed.

The transition between the curves and arcs seems to be abrupt. Fig. 16 indicates a typical time history for the arcs, for $(E, \Theta_0^*, k_0^*) = (0.7, 0, 0.0344)$. This reveals Type 3 character, that is, (i) larger amplitude of x_1 with small modulation, (ii) smaller amplitudes x_2 and x_3 with large modulations, (iii) amplitude modulation period of x_1 just half those of x_2 and x_3, (iv) alternate modulation between x_2 and x_3, and (v) the peak amplitude of x_1 between the peak amplitude of x_2 and that of x_3. Type 3 character is found also for $k_0^* = 0.0349$ and for $k_0^* = 1.0$, but with larger amplitude of x_3 and smaller amplitudes of x_1 and x_2. In contrast, Fig. 17 indicates a typical time history for the merged curves, namely for $k_0^* = 0.0346$: this is characterised by *sudden apparently-random changes of solution type*. Type 3 character (of differing configurations) appears

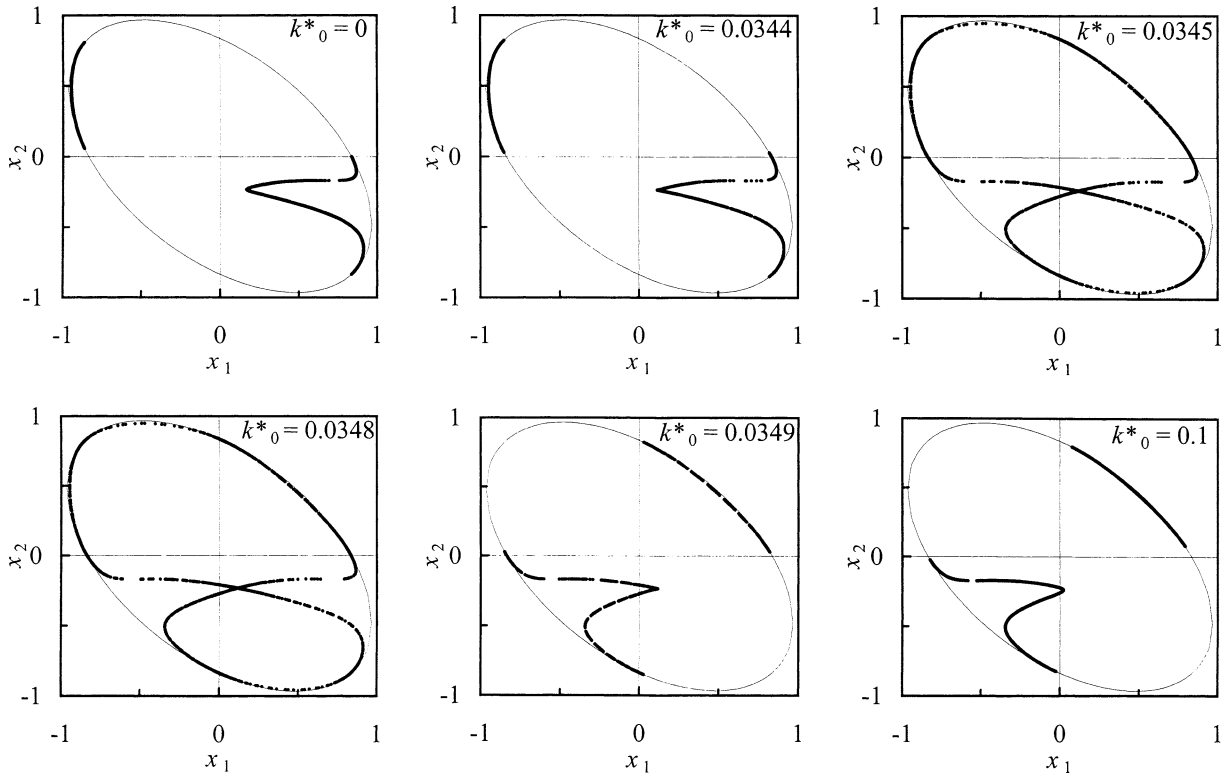

Fig. 14. Poincaré section for $E = 0.7$ and $\Theta_0^* = 0$. In each figure, a thin black line (an ellipse) denotes Eq. (27).

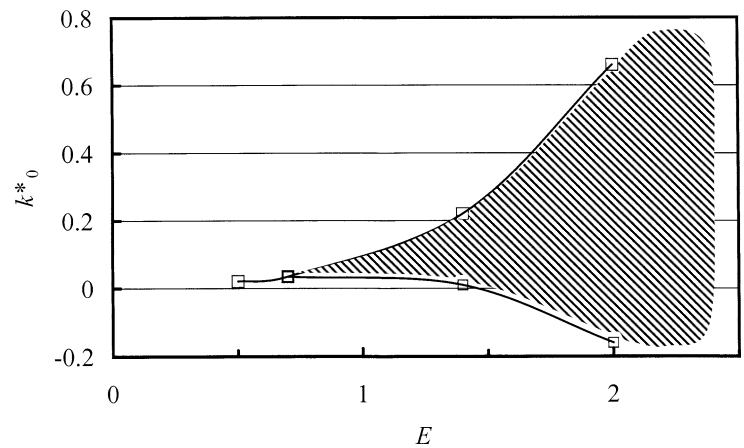

Fig. 15. Chaos region at $\Theta_0^* = 0$ and $k_0^* \approx 0$, where two pairs of arcs in the Poincaré section merge into two joined closed curves.

for $0 < t < 3{,}000$, $3{,}000 < t < 12{,}000$, $25{,}0000 < t < 27{,}000$ and $27{,}000 < t < 30{,}000$. For $12{,}000 < t < 25{,}000$, we can see Type 2 character with (1) the same amplitude and the same period of modulation of x_1, x_2 and x_3, (2) rotation of the large modulations of x_1, x_2 and x_3. It seems that the motion becomes chaotic due to random switching among Type 2 and Type 3 solutions; more precisely, random selection of one among two Type 2's (x_1–x_2–x_3 and x_3–x_2–x_1) and three Type 3's ((x_1, x_2–x_3), (x_2, x_3–x_1) and (x_3, x_1–x_2)). Such chaotic behaviour can be observed in most of the merged-curve region in Fig. 15.

To clarify the question of chaos, Fig. 18 shows the effect of E at $\Theta_0 = 0$ and at $k_0^* \approx 0$. With increasing E, the section becomes complicated, and at $E = 2$ and 2.3, chaotic behaviour is clearly visible, although such large values of E lack physical

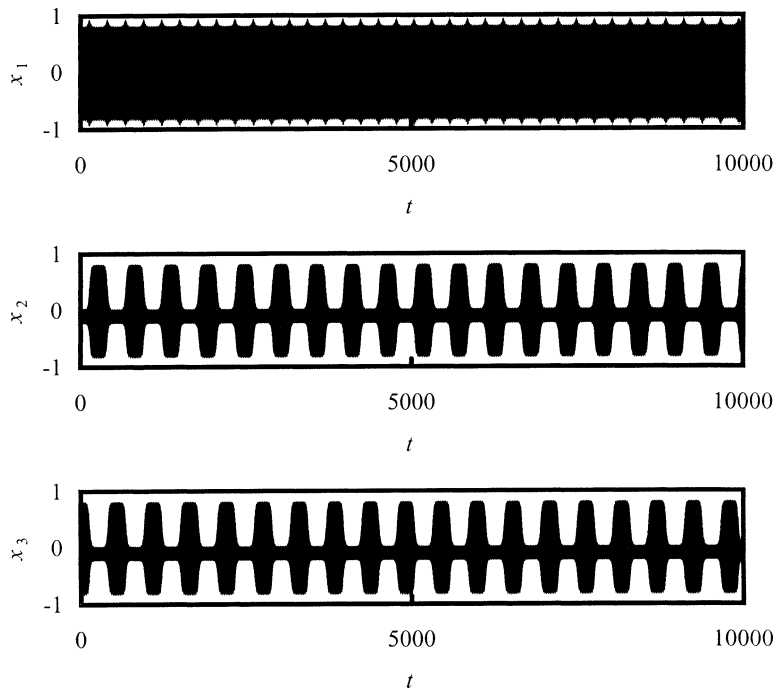

Fig. 16. Time histories for $(E, \Theta_0^*, k_0^*) = (0.7, 0, 0.0344)$.

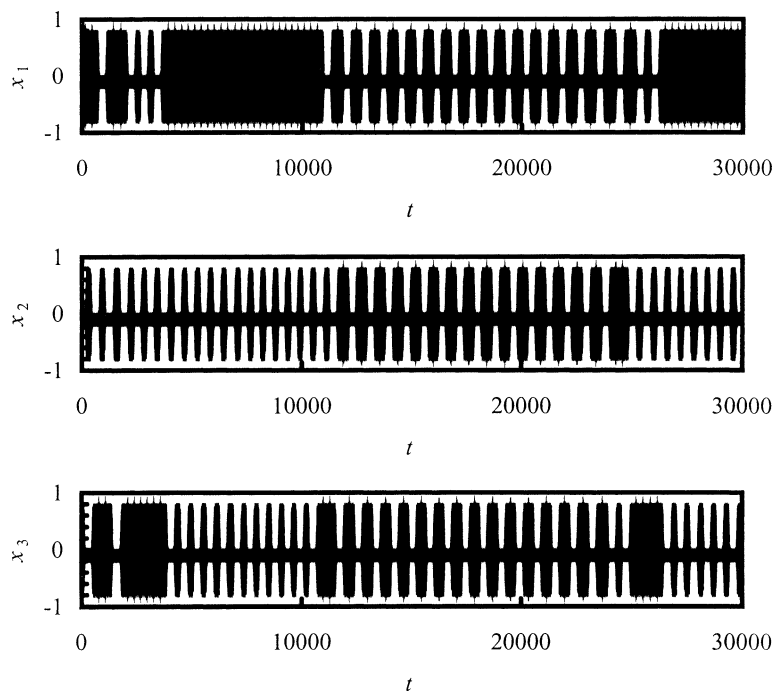

Fig. 17. Time histories for $(E, \Theta_0^*, k_0^*) = (0.7, 0, 0.0346)$.

interpretation. Fig. 19 indicates a typical time history for $E = 2.3$. As expected, irregularity is obvious. However, we can still recognise the random switching among Type 2 and Type 3.

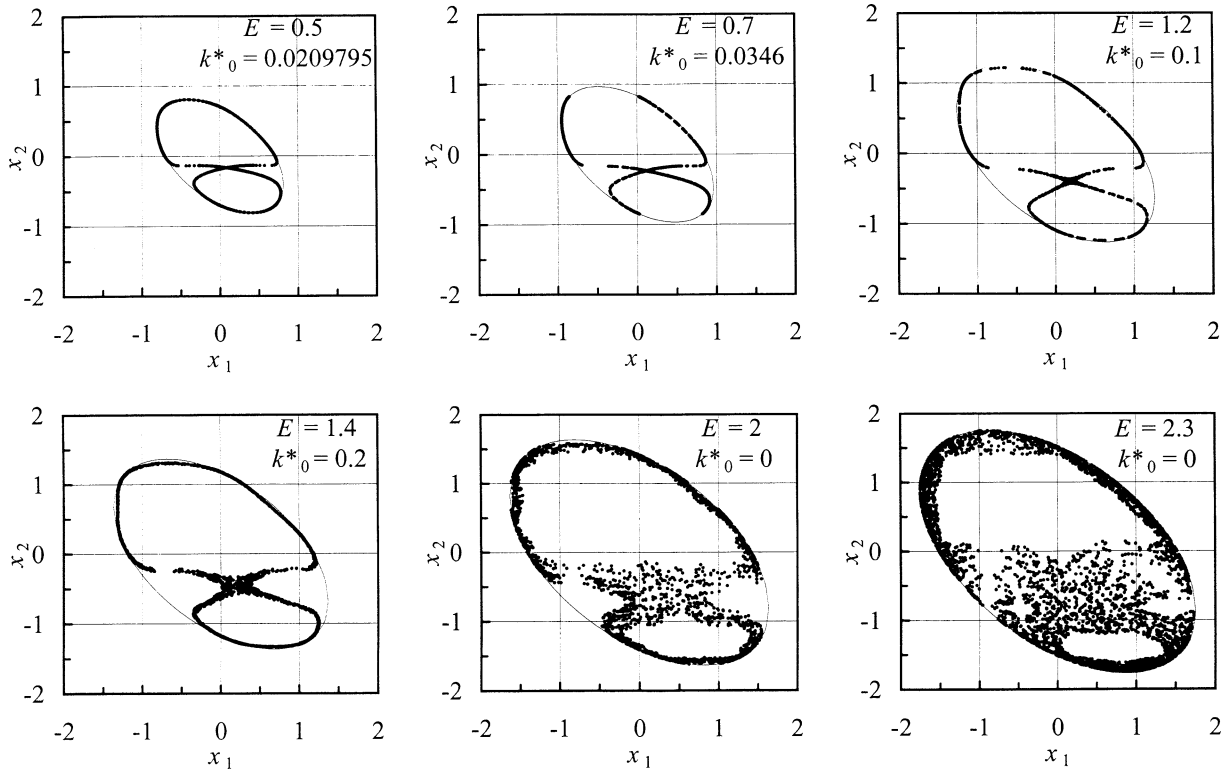

Fig. 18. Poincaré section for $\Theta_0^* = 0$ and $k_0^* \approx 0$. In each figure, a thin black line (an ellipse) denotes Eq. (27).

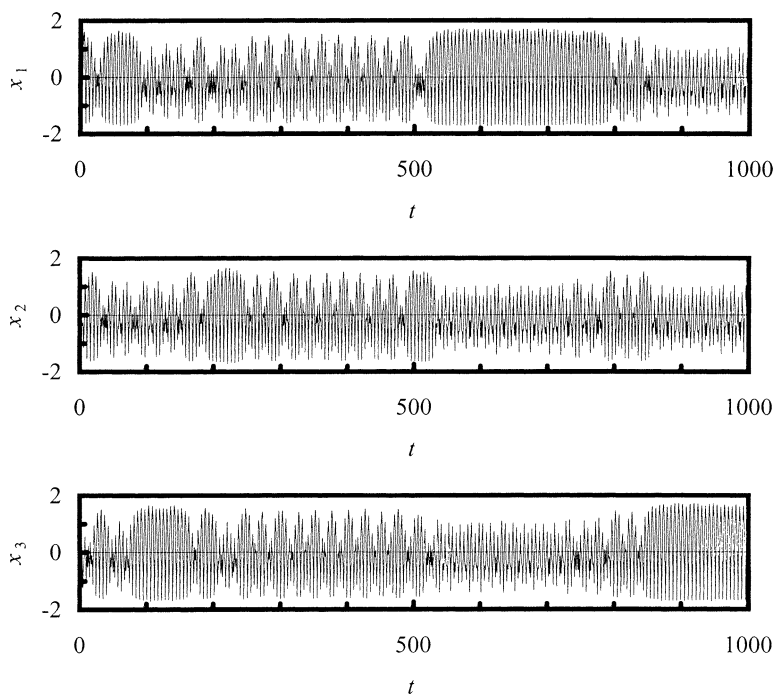

Fig. 19. Time histories for $(E, \Theta_0^*, k_0^*) = (2.3, 0, 0)$.

To help interpret these Poincaré sections, it is instructive to consider the small-amplitude predictions of weakly-nonlinear theory. We have

$$\tilde{x}_j = \varepsilon r_j \exp\bigl[\mathrm{i}(t+\theta_j)\bigr] + \text{c.c.} \quad (j=1,2) \tag{28}$$

and $\dot{\tilde{x}}_2 = 0$ on our chosen Poincaré section. It follows that $t = n\pi - \theta_2$ on the section. Accordingly,

$$\tilde{x}_1 = \varepsilon r_1 \exp\bigl[\mathrm{i}(n\pi + \Theta)\bigr] + \text{c.c.} = \pm 2\varepsilon r_1 \cos\Theta, \qquad \tilde{x}_2 = \pm 2\varepsilon r_2 \tag{29}$$

with corresponding signs. On using results (19)–(23), it follows after some reduction that, on the Poincaré section,

$$(\tilde{x}_1, \tilde{x}_2) = \frac{\pm 2\varepsilon\{F/\sqrt{3} + 2H\sin(\psi' + \pi/3), -2F/3 - (2H/\sqrt{3})\sin\psi'\}}{\sqrt{2F/3 + (2H/\sqrt{3})\sin\psi'}}, \tag{30}$$

where $\psi' \equiv \psi - \pi/3$. Provided $G \neq 0$ and the modulation period is not commensurable with 2π, all such points will appear on the section. With the particular choices $\widetilde{E} = 0.5$ and $\Theta_0 = -\pi/2$ corresponding to Fig. 12(a), this becomes

$$(\tilde{x}_1, \tilde{x}_2) = \pm\left\{\frac{1/2 + \tilde{\kappa}\sin(\psi' + \pi/3)}{\sqrt{3}\sqrt{1 + \tilde{\kappa}\sin\psi'}}, -\frac{1}{\sqrt{3}}\sqrt{1 + \tilde{\kappa}\sin\psi'}\right\}, \tag{31}$$

where

$$\tilde{\kappa} \equiv \frac{\sqrt{1 - k_0^2 + k_0^4}}{1 + k_0^2} \tag{32}$$

and $k_0 \equiv r_{20}/r_{10}$. The points (31) are shown in Fig. 12(a) as thick grey lines, which compare quite well with the full nonlinear computations (black dots). Smaller E gives still better agreement: for example, the curves nearly coincide for E less than about 0.05.

The broad similarity of these results with Poincaré sections of Fig. 12(a) is clear, though there are differences attributable to the higher harmonics neglected from the weakly-nonlinear estimates. But weakly-nonlinear theory cannot predict the behaviour shown in Figs. 17–19, which shows evidence of chaos. This is because the full nonlinear equations possess one less constant of motion than does the weakly-nonlinear system: a similar situation is encountered with the Hénon–Heiles equations [12] (we are grateful to Prof. T. Kawahara of Kyoto University for pointing our this similarity).

Weakly-nonlinear theory does not well represent the Poincaré sections of Fig. 12(b), since these correspond to cases with $G = 0$ and so have an 'infinite modulation period'. The initial data in these cases correspond to the marginally-stable solutions FP1 of (15)–(17). In Fig. 10, we found evidence that the solution trajectories still remain fairly close to a *portion* of the elliptical curve predicted by weakly-nonlinear theory; but neither this ellipse, nor the corresponding Poincaré sections as in Fig. 12(b), are then usually traversed in full. It is higher-order nonlinear terms which control the departures from the initial marginally-stable fixed points FP1 in such cases.

We are convinced that the region of chaos is a genuine physical phenomenon, rather than a numerical artifact resulting from inaccuracies inherent in our Runge–Kutta scheme. Certainly, chaos is normally to be expected precisely when orbits pass close to heteroclinic points, as they do here. But, in all realisable cases (for which no tube becomes empty), the region of chaos in parameter space is very thin and the time-scale over which it becomes apparent is rather large. In such cases, it is possible that very small numerical inaccuracies may significantly affect the computed solutions. In particular, the Runge–Kutta scheme does not conserve energy *precisely*, though checks revealed that the energy did indeed remain very nearly constant throughout. Further computations, performed with the different time steps 5×10^{-3}, 10^{-3}, 5×10^{-4} and 10^{-4}, all yielded the *same* region of chaos shown in Fig. 15, even though individual solution trajectories were not the same in this region. Accordingly, we cannot *prove* that our method is then sufficiently accurate; but we are hopeful that it is. We are aware that special numerical methods, for example multi-step methods such as symplectic integration, exist for the detection of transitions to chaos (we thank Prof. D.G. Dritschel and a referee for this suggestion). But, as this was not the main purpose of our paper, any such extensions must be left for the future.

4.6. Amplitude and period of modulations

To obtain a more global view of the modulating solutions, we have investigated the dependence on governing parameters of both the amplitude and the period of modulations. The period of modulations was estimated by recording the successive times of greatest amplitude for x_1 over several periods. We defined our measure of amplitude modulations as the 'amplitude modulation ratio'

$$\frac{(\|x_1\|_{\max} - \|x_1\|_{\min}) + (\|x_2\|_{\max} - \|x_2\|_{\min}) + (\|x_3\|_{\max} - \|x_3\|_{\min})}{(\|x_1\|_{\max} + \|x_1\|_{\min})/2 + (\|x_2\|_{\max} + \|x_2\|_{\min})/2 + (\|x_3\|_{\max} + \|x_3\|_{\min})/2},$$

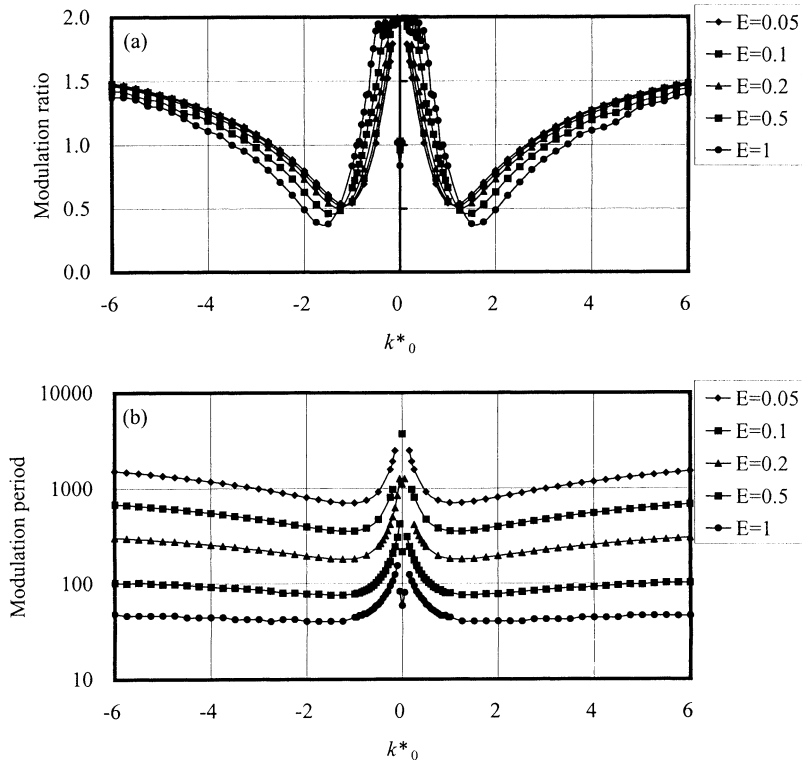

Fig. 20. Results against k_0^* for $\Theta_0^* = -\pi/2$ and various E. (a) Amplitude modulation ratio, (b) amplitude modulation period.

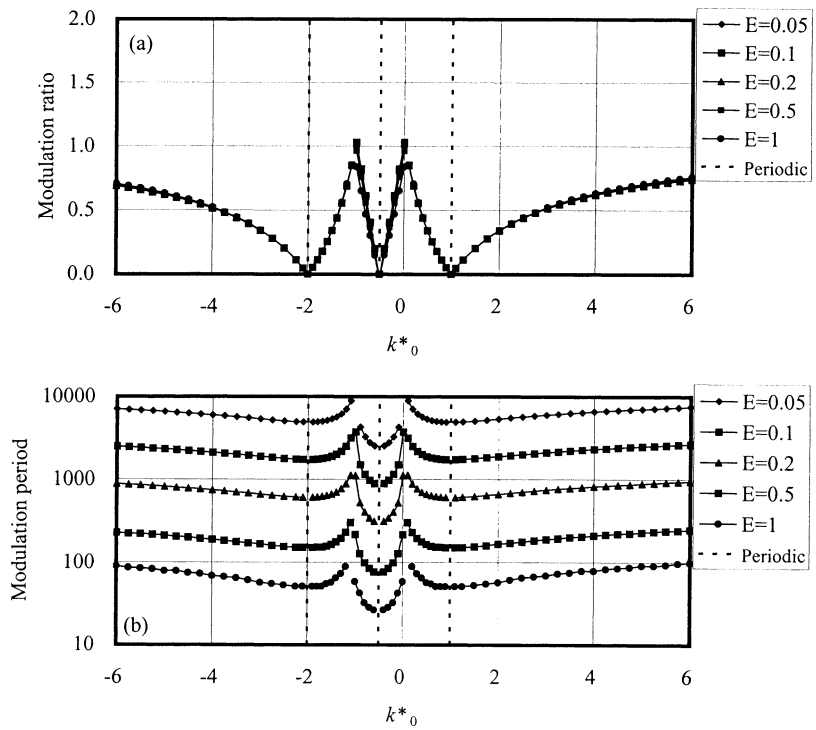

Fig. 21. Results against k_0^* for $\Theta_0^* = 0$ and various E. (a) Amplitude modulation ratio, (b) amplitude modulation period.

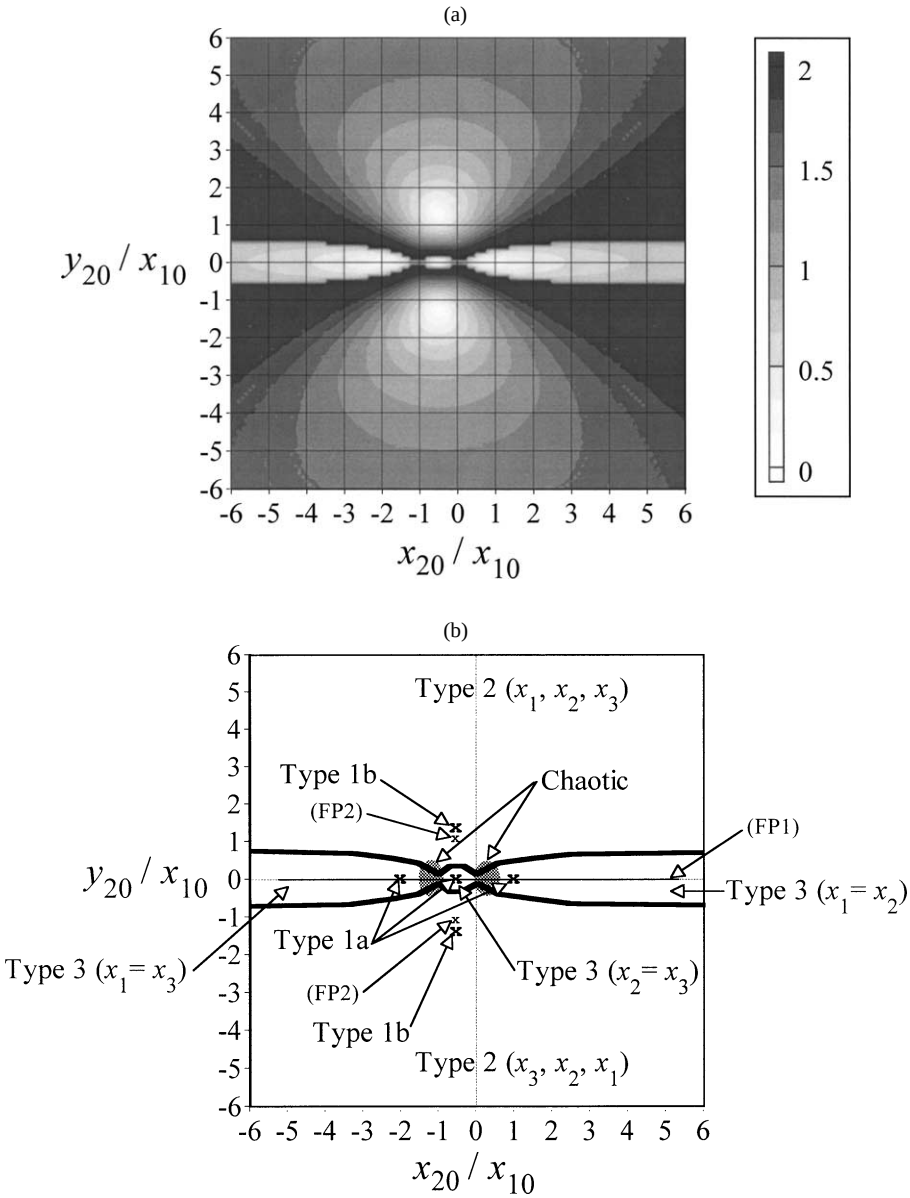

Fig. 22. Contour map of amplitude modulation ratio, at fixed $E = 0.5$. (a) Contour map, (b) line sketch.

Table 1
Summary of solutions and their characteristics

Type 1a	Periodic with zero phase shift. 3 cases, $x_1 = x_2,\ x_2 = x_3,\ x_3 = x_1$ where $x_3 = -x_1 - x_2$.
Type 1b	Periodic with relative $2\pi/3$ phase shifts and equal amplitudes. 2 cases, cycling $x_1 \to x_2 \to x_3$, or $x_3 \to x_2 \to x_1$.
Type 2	Slow out-of-phase periodic modulations about Type 1b, in two separate large regions with $\dot{x}_{20}/x_{10} \gtrapprox 0.5$ and $\lessapprox -0.5$.
Type 3	Slow in-phase periodic modulations about Type 1a, in three quite small regions within $\lvert\dot{x}_{20}/x_{10}\rvert \lessapprox 0.5$.
Chaotic	Chaotic modulations in two very small regions close to $(x_{20}/x_{10}, \dot{x}_{20}/x_{10}) = (0, 0)$ and $(-1, 0)$.

where $\|x_j\|$ is a *positive* value of x_j at times such that $\dot{x}_j = 0$ ($j = 1, 2, 3$). Subscripts 'max' and 'min' are the greatest and least recorded values of $\|x_1\|$, $\|x_2\|$ and $\|x_3\|$, over a suitably large computational time.

Results for the amplitude modulation ratio and the amplitude modulation period are shown in Figs. 20(a), 20(b) for Type 2 solutions with $\Theta_0^* = -\pi/2$ and $-6 \leqslant k_0^* \leqslant 6$ with various fixed E. Corresponding results for Type 3 solutions with $\Theta_0^* = 0$ are shown in Figs. 21(a), 21(b). There is no modulation for $k_0^* = 1$, -0.5 or -2 since these correspond to Type 1a periodic solutions. For Type 3, the modulation period is roughly proportional to $E^{-3/2}$ for each fixed k_0^*; but for Type 2 the proportionality seems closer to E^{-1}. On the other hand, for both of Type 2 and 3, the amplitude modulation ratio is less affected by the value of E than is the modulation period. Similar curves were found for other values of Θ_0^*, but these are not shown.

Instead, Fig. 22(a) shows a contour map of the modulation ratio at fixed $E = 0.5$, which has features similar to that of the modulation period. Fig. 22(b) is a line sketch of the contour map, showing the distribution of solutions, with each type described in Table 1. Here, the abscissa is $x_{20}/x_{10} = k_0^* \cos\Theta_0^*$, and the ordinate is $\dot{x}_{20}/x_{10} = k_0^* \sin\Theta_0^*$. Of course, this kind of contour map can be affected by E; especially, the modulation period is sensitive to E, although the modulation ratio is not.

Three features described below are robustly maintained at realisable values of E. (i) There are 'ridges' at $(x_{20}/x_{10}, \dot{x}_{20}/x_{10}) \approx$ (arbitrary, ± 0.5), which are shown by thick lines in Fig. 22(b). These ridges are considered to be related to FP1 on $\Theta_0^* = 0$ (or on $\dot{x}_{20}/x_{10} = 0$). (ii) There are five troughs at $(x_{20}/x_{10}, \dot{x}_{20}/x_{10}) = (1, 0), (-1/2, 0), (-2, 0)$ and near $(-0.5, \pm 1.3)$, where the modulation ratio is 0 and the modulation period is $+\infty$. The first three are related to Type 1a periodic solutions, and the last two are related to Type 1b periodic solutions. The last two differ somewhat from the weakly-nonlinear fixed points FP2 (modulo 2π), that is, $(x_{20}/x_{10}, \dot{x}_{20}/x_{10}) = (-1/2, -\sqrt{3}/2)$ and $(-1/2, \sqrt{3}/2)$, because of stronger nonlinearity. (iii) There are three saddle points near $(x_{20}/x_{10}, \dot{x}_{20}/x_{10}) = (0, 0), (-1, 0)$ and $(\pm\infty, \pm\infty)$, that is, near $(k_0^*, \Theta_0^*) = (0,$ arbitrary$), (-1, 0)$ and $(\pm\infty,$ arbitrary$)$.

Using this contour map, we can also roughly envisage the regions of Type 2 and 3 modulations. The ridges are almost boundaries between Type 2 and 3; that is, Type 2 modulations occur in broad areas beyond the ridges, but Type 3 modulations are restricted within narrow areas between the ridges. More specifically, we can see Type 2 (x_1–x_2–x_3) modulation at $\dot{x}_{20}/x_{10} \gtrapprox 0.5$, and Type 2 ($x_3$–$x_2$–$x_1$) modulation at $\dot{x}_{20}/x_{10} \lessapprox -0.5$. Between $\dot{x}_{20}/x_{10} \approx \pm 0.5$, we can see Type 3 ($x_3$, x_1–x_2) modulation at $x_{20}/x_{10} \gtrapprox 0$, Type 3 ($x_1$, x_2–x_3) modulation at $-1 \lessapprox x_{20}/x_{10} \lessapprox 0$, and Type 3 ($x_2$, x_3–x_1) modulation at $x_{20}/x_{10} \lessapprox -1$. Chaotic behaviours are observed in very small regions near $(x_{20}/x_{10}, \dot{x}_{20}/x_{10}) \approx (0, 0)$ and $(-1, 0)$: these are exaggerated in Figs. 22(a), 22(b) to make them visible. From the contour map, we can confirm that each chaotic region is near boundaries of two Type 2 solutions and two Type 3 solutions. Furthermore, from Fig. 22, it is seems natural that exactly periodic solutions of Type 1a and Type 1b are special (unmodulating) cases of Type 3 and Type 2, respectively.

5. Other tube configurations

The above analysis may be extended to other arrangements of three tubes which are smoothly joined at their bases. Here, we consider that each tube is characterised by its length L_j ($j = 1, 2, 3$), its cross-sectional area S_j, supposed uniform throughout its length, and the constant angle α_j of inclination of its 'working section' to the vertical. By 'working section' we mean that portion of the tube within which the liquid surface is supposed always to lie: thus, the component of gravitational acceleration $g \sin\alpha_j$ acting along each tube is a constant, but the tube itself may be curved in any manner below the working section. Without loss, we may non-dimensionalise with respect to the length of one tube. Also, since it is only the *ratios* of the cross-sections S_j which matter, we may set one of the S_j to unity without loss. For definiteness, we suppose that tube 3 has the shortest length, which we choose as the length-scale for non-dimensionalisation: then L_1 and $L_2 \geqslant 1$ represent the lengths of tubes 1 and 2 relative to that of tube 3. Similarly, we set $S_3 = 1$, so that S_1 and S_2 are the cross-sections of tubes 1 and 2 relative to that of tube 3. In our dimensionless variables, each component of gravity is represented by $\sin\alpha_j \equiv s_j$.

Denoting by x_j the three dimensionless surface displacements *along each tube*, measured upwards from equilibrium, we have the continuity condition

$$S_1 x_1 + S_2 x_2 + S_3 x_3 = 0,$$

which suggests the introduction of new variables

$$z_j \equiv S_j x_j \quad (j = 1, 2, 3),$$

with $z_3 = -z_1 - z_2$. Then, the potential energy V and kinetic energy T are given by

$$2V(x_i) = \sum_{j=1}^{3} (S_j \sin\alpha_j) {x_j}^2 = \sum_{j=1}^{3} \frac{s_j}{S_j} {z_j}^2,$$

$$2T(\dot{x}_i, x_i) = \sum_{j=1}^{3} \dot{x}_j{}^2 (L_j + x_j) S_j = \sum_{j=1}^{3} \frac{\dot{z}_j{}^2 (S_j L_j + z_j)}{S_j{}^2}.$$

On eliminating z_3 and setting $S_3 = 1$, we obtain

$$2V(z_i) = \frac{s_1}{S_1} z_1{}^2 + \frac{s_2}{S_2} z_2{}^2 + s_3 (z_1 + z_2)^2,$$

$$2T(\dot{z}_i, z_i) = \dot{z}_1{}^2 \left[z_1 \left(\frac{1}{S_1{}^2} - 1 \right) - z_2 + \frac{L_1}{S_1} + 1 \right] + \dot{z}_2{}^2 \left[z_2 \left(\frac{1}{S_2{}^2} - 1 \right) - z_1 + \frac{L_2}{S_2} + 1 \right] + 2\dot{z}_1 \dot{z}_2 (1 - z_1 - z_2),$$

from which the Lagrangian $L \equiv T - V$ is obtained in terms of z_1, z_2 and their derivatives.

Lagrange's equations yield

$$\ddot{z}_1 (l_1 l_2 + l_1 + l_2) + z_1 \big[(l_2 + 1)\sigma_1 + l_2 \sigma_3 \big] + z_2 [l_2 \sigma_3 - \sigma_2] = \frac{1}{2} N_1, \tag{33}$$

$$\ddot{z}_2 (l_2 l_1 + l_2 + l_1) + z_2 \big[(l_1 + 1)\sigma_2 + l_1 \sigma_3 \big] + z_1 [l_1 \sigma_3 - \sigma_1] = \frac{1}{2} N_2, \tag{34}$$

where we have defined $l_i \equiv L_i / S_i$ $(i = 1, 2)$ and $\sigma_j \equiv s_j / S_j$ $(j = 1, 2, 3)$. Recall, too, that we have set $L_3 = S_3 = 1$ without loss. Here, N_1 and N_2 denote nonlinear terms, the former being

$$\begin{aligned} N_1 \equiv\ & 2\ddot{z}_1 z_1 \big[l_2 - S_1{}^{-2} (l_2 + 1) \big] + 2 l_2 (\ddot{z}_1 z_2 + \ddot{z}_2 z_1) + 2\ddot{z}_2 z_2 \big(l_2 + S_2{}^{-2} \big) \\ & + \dot{z}_1{}^2 \big[l_2 - S_1{}^{-2} (l_2 + 1) \big] + 2 l_2 \dot{z}_1 \dot{z}_2 + \dot{z}_2{}^2 \big(l_2 + S_2{}^{-2} \big) \end{aligned} \tag{35}$$

and that for N_2 having subscripts 1 and 2 interchanged.

For small oscillations, the N_j may be set to zero in (33) and (34) to obtain the form and frequencies of the two linear modes. Unlike the degenerate configuration studied above, the two frequencies are normally distinct, and each is associated with a particular form of motion. Denoting the unknown frequencies by ω, we have

$$\omega^4 (l_1 l_2 + l_1 + l_2) - \omega^2 \big[l_1 (\sigma_2 + \sigma_3) + l_2 (\sigma_3 + \sigma_1) + (\sigma_1 + \sigma_2) \big] + (\sigma_1 \sigma_2 + \sigma_2 \sigma_3 + \sigma_3 \sigma_1) = 0. \tag{36}$$

The roots of this quadratic equation are easily found, together with the ratios $z_1 : z_2$ of the corresponding oscillations with either frequency, which are

$$\big[\omega^2 (l_1 l_2 + l_1 + l_2) - l_1 \sigma_2 - l_1 \sigma_3 - \sigma_2 \big] : [l_1 \sigma_3 - \sigma_1].$$

Note that the frequencies depend on the five parameters l_i, σ_j, but that the nonlinear terms involve the two further parameters S_1 and S_2.

Weakly-nonlinear interactions between the two modes are normally governed by equations of the form

$$2\mathrm{i} \frac{\mathrm{d}A_1}{\mathrm{d}T} = A_1 \big(a_1 |A_1|^2 + b_1 |A_2|^2 \big), \qquad 2\mathrm{i} \frac{\mathrm{d}A_2}{\mathrm{d}T} = A_2 \big(a_2 |A_2|^2 + b_2 |A_1|^2 \big), \tag{37}$$

correct to $\mathrm{O}(\varepsilon^3)$, in the notation of Section 2 above. The real coefficients $a_i,\ b_i$ $(i = 1, 2)$ may be found by performing a routine but lengthy nonlinear expansion, but this is not done here. The additional terms present in Eqs. (11) and (12) arose because the two frequencies are there identical, and here they are considered to differ by an O(1) amount. But exceptional cases arise when the two frequencies are close to either 1:1 or 1:2 resonance. In the former case, equations like (11) and (12) will apply at exact resonance; but a small $\mathrm{O}(\varepsilon^2)$ frequency-mismatch introduces additional T-dependent factors: see, for example, Umeki and Kambe [13] or Craik [14] for discussions of the analogous situation of water waves near 1:1 resonance.

The condition for exact 1:1 resonance may be derived from (36). This is

$$\begin{aligned} & (l_1 \rho_2)^2 + (l_2 \rho_1)^2 + 2 \big[l_1 \rho_2 (l_1 + \rho_2) + \rho_1 l_2 (\rho_1 + l_2) \big] + (l_1 + l_2)^2 + (\rho_1 + \rho_2)^2 \\ & \quad = 2 (l_1 l_2 + l_1 + l_2)(\rho_1 \rho_2 + \rho_1 + \rho_2). \end{aligned} \tag{38}$$

Similarly, the condition for exact 1:2 resonance is found to be

$$25 (l_1 l_2 + l_1 + l_2)(\rho_1 \rho_2 + \rho_1 + \rho_2) = 4 (l_1 \rho_2 + l_2 \rho_1 + l_1 + l_2 + \rho_1 + \rho_2)^2. \tag{39}$$

In (38) and (39), $\rho_i \equiv \sigma_i / \sigma_3 \equiv s_i S_3 / s_3 S_i$ $(i = 1, 2)$ and $S_3 = 1$. Note that these resonance conditions depend on only four parameters. If any three are given, Eqs. (38) and (39) yield quadratic equations for the fourth. There is symmetry with respect to the l_i and ρ_i, as well as the subscripts 1 and 2. Among cases when 1:1 resonance occurs are all those with $l_1 = l_2 = \rho_1 = \rho_2$. The weakly-nonlinear equations for 1:1 resonance must resemble (11) and (12) in form, but the coefficients may differ.

In order to obtain some insight into the likelihood of 1:2 resonance, we note some particular solutions of (39): (a) $l_1 = l_2 = 1$, $\rho_1 = 1$, $\rho_2 = 11/2$; (b) $l_1 = l_2 = 1$, $\rho_1 = \rho_2 = 2/11$, and six more corresponding solutions obtained by interchanging subscripts 1, 2 and/or variables l_i, ρ_i. Also, more generally, (A) if $l_1 = l_2 = \rho_1 \equiv l$ and $\rho_2 \equiv \rho$, the quadratic roots are

$$\rho = \frac{l(l-2)}{4(l+1)}, \frac{l(4l+7)}{l+1}, \tag{40}$$

(B) if $l_1 = l_2 \equiv l$ and $\rho_1 = \rho_2 \equiv \rho$, the quadratic roots are

$$\rho = \frac{2l}{3l+8}, \frac{8l}{2-3l}, \tag{41}$$

which must be positive. It is clear that 1:2 resonance can occur in realisable cases. For instance, with tubes of equal cross-sections S_j, one possible configuration has tube 3 vertical ($L_3 = s_3 = 1$), and tubes 1 and 2 that are four times as long ($L_1 = L_2 = l = 4$) with working sections inclined at the angle $\sin^{-1}(2/5)$ ($\rho = 2/5$), or about 23.6° to the horizontal. Such a configuration could be realised by a short vertical tube ($L_3 = 1$) and two long bent tubes ($L_1 = L_2 = 4$) comprising horizontal sections of length 1.5 and inclined sections of length 2.5 at the required angle $\sin^{-1}(2/5)$.

At exact 1:2 resonance, the weakly-nonlinear equations contain quadratic terms: see, for example, Craik [10], Miles and Henderson [15], Forster and Craik [16] or Craik, Okamoto and Allen [20] for full discussion of analogous cases for water waves and coupled pendula. When the linear frequency of mode A_2 is twice that of mode A_1, these have the form, at $O(\varepsilon^2)$,

$$2\mathrm{i}\frac{\mathrm{d}A_1}{\mathrm{d}T_m} = p_1 A_2 \bar{A}_1, \qquad 2\mathrm{i}\frac{\mathrm{d}A_2}{\mathrm{d}T_m} = p_2 {A_1}^2, \tag{42}$$

where $T_m \equiv \varepsilon t$ is a faster timescale than $T \equiv \varepsilon^2 t$ above. Cubic terms such as those of (37) will arise as $O(\varepsilon)$ corrections to these. A fuller account of such systems is in preparation.

6. Discussion

We have described the evolution of inviscid gravitational oscillations in configurations of three tubes. Linear and weakly-nonlinear approximate theories successfully describe some aspects of the exact solutions which were found numerically. In particular, the frequency of oscillations is always close to that predicted by simple linear theory. Once we introduce a classification of Type 1a, 1b, 2 and 3, the prediction becomes more precise. Here, the frequencies in Type 1a can be got analytically, and the frequencies in Type 1b, 2 and 3 are well estimated by weakly-nonlinear theory. The frequencies of nonlinear modulations, on a longer timescale, are also fairly accurately described by our weakly-nonlinear theory based on truncated amplitude equations. Indeed, it would be possible to pursue weakly-nonlinear theory to higher orders of approximation. For example, incorporation of forced second-harmonic contributions proportional to B_1 in (9) and B_2 in (10) would improve the agreement between theory and direct computation in Figs. 8 and 10, where second harmonics are evident. However, these truncated equations possess one more invariant of motion than do the full equations, and so are unable to capture the chaotic behaviour which arises in a narrow region of parameter space. The nature of this chaos is, broadly, a random switching between two types of almost-periodic modulations, with characteristic structures identified above as Type 2 and Type 3. This random switching seems to be localised in the vicinity of heteroclinic orbits.

Our unforced, inviscid system is conservative and Hamiltonian. But viscosity, or other damping agent, may have a marked effect on any real configuration. To counteract the inevitable loss of energy due to damping, one might introduce periodic forcing. This is done in Faraday excitation of standing water waves, where the whole tank containing liquid is oscillated vertically at nearly twice the frequency of the dominant wave modes. In our case, the tubes might be oscillated vertically on a supporting frame. The literature on Faraday waves is huge and rapidly-growing: see, for instance, the reviews of Miles and Henderson [15] and Craik [14].

In the present context, is reasonable to expect that the presence of weak damping and excitation will have effects broadly similar to those for Faraday waves, since the weakly-nonlinear governing equations must take a similar form. It is possible that Hamiltonian chaos will be eliminated; but other potential sources of modulation and chaos will be introduced through linear and nonlinear detuning relative to the imposed driving frequency. Finite-amplitude periodic oscillations may then display hysteresis or limit-cycle behaviour. Furthermore, the parameter domains of hysteresis can be influenced by nonlinear damping or by higher-order frequency modification, as in the work of Decent and Craik [11,17,18] and Martel, Knobloch and Vega [19]. Second-harmonic resonance can occur in both systems, when suitably set up: cf. Craik, Okamoto and Allen [20] and references therein. The influence of viscous and turbulent damping of oscillations in a U-tube has already been considered by Tanigawa, Hirata and Yano [21]. Further theoretical work along these lines is left for the future. But, with three tubes, reduction of energy losses, and elimination of any preferential bias where the tubes are joined, may prove experimentally difficult.

A three-tube configuration has one major advantage over a Faraday wave tank: namely, the only possible motions are those described by our coupled equations (1), (2), suitably extended to include damping and forcing. In contrast, the theoretical restriction to a small set of dominant standing Faraday modes can be violated by spontaneous generation of other neighbouring modes, so increasing the degrees of freedom of the system. We therefore recommend the three-tube configuration as a promising experimental test-bed for low-dimensional dynamical systems. We look forward to hearing from anyone who takes up the challenge.

References

[1] D. Bernoulli, Hydrodynamica, sive de viribus et motibus fluidorum commentarii, Joh. Reinholdi Dulseckeri, Argentorati (Strasbourg), 1738.
[2] I.S. Gradshteyn, I.W. Ryzhik, Tables of Integrals, Series, and Products, 4th edition, Academic Press, New York, 1965.
[3] M. Abramowitz, I.A. Stegun (Eds.), Handbook of Mathematical Functions, Dover, New York, 1965.
[4] A.H. Nayfeh, Perturbaton Methods, Wiley, New York, 1973.
[5] M. Nagata, Nonlinear Faraday resonance in a box with square base, J. Fluid Mech. 209 (1989) 265–284.
[6] M. Umeki, Faraday resonance in rectangular geometry, J. Fluid Mech. 227 (1991) 161–192.
[7] S. Douady, S. Fauve, O. Thual, Oscillatory phase modulation of parametrically forced surface waves, Europhys. Lett. 10 (4) (1989) 309–315.
[8] G. Danglemayr, E. Knobloch, Hopf bifurcation with broken symmetry, Nonlinearity 4 (1991) 399–427.
[9] M. Golubitsky, I. Stewart, D.G. Schaeffer, Singularities and Groups in Bifurcation Theory, Vol. 2, Springer, New York, 1988.
[10] A.D.D. Craik, Wave Interactions and Fluid Flows, Cambridge University Press, Cambridge, 1985.
[11] S.P. Decent, A.D.D. Craik, Hysteresis in Faraday resonance, J. Fluid Mech. 293 (1995) 237–268.
[12] M. Hénon, C. Heiles, The applicability of the third integral of motion: some numerical experiments, Astronomical J. 69 (1964) 73–79.
[13] M. Umeki, T. Kambe, Nonlinear dynamics and chaos in parametrically excited surface waves, J. Phys. Soc. Japan 58 (1989) 140–154.
[14] A.D.D. Craik, Nonlinear interaction of standing waves with Faraday excitation, in: L. Debnath, D.N. Riahi (Eds.), Nonlinear Instability, Chaos and Turbulence, Vol. 1, Chapter 4, WIT Press, Southampton, UK, 1998, pp. 91–128.
[15] J.W. Miles, D.M. Henderson, Parametrically forced surface waves, Ann. Rev. Fluid Mech. 22 (1990) 143–165.
[16] G.K. Forster, A.D.D. Craik, Second-harmonic resonance with Faraday excitation, Wave Motion 26 (1997) 361–377.
[17] S.P. Decent, A.D.D. Craik, On limit cycles arising from the parametric excitation of standing waves, Wave Motion 25 (1997) 275–294.
[18] S.P. Decent, A.D.D. Craik, Sideband instability and modulations of Faraday waves, Wave Motion 30 (1999) 43–55.
[19] C. Martel, E. Knobloch, J.M. Vega, Dynamics of counterpropagating waves in parametrically forced systems, Phys. D 137 (2000) 94–123.
[20] A.D.D. Craik, H. Okamoto, H.R. Allen, Second-harmonic resonance with parametric excitation and damping, in: J.L. Lumley (Ed.), Fluid Mechanics and the Environment: Dynamical Approaches, Springer, Berlin, 2001, pp. 63–89.
[21] H. Tanigawa, K. Hirata, H. Yano, Nonlinear oscillations of liquid column in a U-tube, Nagare 17 (1998) 368–372 (in Japanese).